OzDES Reverberation Mapping Program: Stacking analysis with Hβ, Mg II, and C IV

U. Malik [1]*, R. Sharp,[1]* A. Penton [2], Z. Yu,[3] P. Martini,[3,4] B. E. Tucker,[1,5,6] T. M. Davis [2], G. F. Lewis [7], C. Lidman [1,8] M. Aguena,[9] O. Alves,[10] J. Annis,[11] J. Asorey [12], D. Bacon,[13] D. Brooks,[14] A. Carnero Rosell [9,15,16] J. Carretero [17], T.-Y. Cheng [18] L. N. da Costa,[9] M. E. S. Pereira,[19] J. De Vicente [20], P. Doel,[14] I. Ferrero [21], J. Frieman,[11,22] G. Giannini,[17] D. Gruen [23], R. A. Gruendl [24,25] S. R. Hinton [2], D. L. Hollowood [26], D. J. James,[27] K. Kuehn,[28,29] J. L. Marshall,[30] J. Mena-Fernández,[20] F. Menanteau,[24,25] R. Miquel,[17,31] R. L. C. Ogando [32], A. Palmese [33], A. Pieres [9,32] A. A. Plazas Malagón [34,35] K. Reil,[35] A. K. Romer,[36] E. Sanchez [20], M. Schubnell,[10] M. Smith [37], E. Suchyta [38], M. E. C. Swanson,[14] G. Tarle,[10] C. To,[4] N. Weaverdyck [10,39] and P. Wiseman [37]

Affiliations are listed at the end of the paper

ABSTRACT

Reverberation mapping is the leading technique used to measure direct black hole masses outside of the local Universe. Additionally, reverberation measurements calibrate secondary mass-scaling relations used to estimate single-epoch virial black hole masses. The Australian Dark Energy Survey (OzDES) conducted one of the first multi-object reverberation mapping surveys, monitoring 735 AGN up to $z \sim 4$, over 6 years. The limited temporal coverage of the OzDES data has hindered recovery of individual measurements for some classes of sources, particularly those with shorter reverberation lags or lags that fall within campaign season gaps. To alleviate this limitation, we perform a stacking analysis of the cross-correlation functions of sources with similar intrinsic properties to recover average composite reverberation lags. This analysis leads to the recovery of average lags in each redshift-luminosity bin across our sample. We present the average lags recovered for the Hβ, Mg II, and C IV samples, as well as multiline measurements for redshift bins where two lines are accessible. The stacking analysis is consistent with the Radius–Luminosity relations for each line. Our results for the Hβ sample demonstrate that stacking has the potential to improve upon constraints on the R–L relation, which have been derived only from individual source measurements until now.

Key words: galaxies: active – galaxies: nuclei – quasars: emission lines – quasars: general – quasars: supermassive black holes.

1 INTRODUCTION

Reverberation mapping is a powerful technique that can resolve the cores of active galactic nuclei (AGN) in the time domain. The accretion disc around the central supermassive black hole (SMBH) produces intrinsically variable emission at UV-optical wavelengths. The surrounding broad-line region (BLR) is ionized by this continuum emission, which drives a reverberation response in the emission-line flux from the BLR on time-scales of weeks to months (Blandford & McKee [1982](); Peterson [1993]()). Multi-epoch photometric and spectroscopic observations can be used to trace the variability of the continuum and the emission-line response, respectively.

The size difference between the accretion disc (light-days to weeks) and the BLR (light-weeks to months) introduces a delay in the response of the BLR to the variation in the ionizing flux. The delay,

i.e. reverberation lag, τ, can be recovered by cross-correlating the two light curves, in order to measure the radius of the BLR ($R_{\mathrm{BLR}} = c\tau$). The velocity dispersion of the BLR (ΔV) can be estimated from the width of the broadened emission lines. The mass of the central black hole (M_{BH}) can then be measured using the virial theorem:

$$M_{\mathrm{BH}} = f \frac{R_{\mathrm{BLR}} \Delta V^2}{G}, \tag{1}$$

where f is the virial coefficient; a dimensionless scale factor that accounts for the geometry, orientation, and kinematics of the BLR (Woo et al. [2015]()).

Reverberation mapping (RM) is presently the only method that can be used to directly measure SMBH masses beyond the local Universe, as other techniques are reliant on resolving the gravitational sphere-of-influence of the black hole, which remains challenging even with high-angular resolution instruments (e.g. Gebhardt et al. [2000](), [2011](); Kuo et al. [2011](); Event Horizon Telescope Collaboration et al. [2019]()). However, RM is by nature observationally intensive. It requires repeated observation over the relevant variability time-scales of AGN

* E-mail: umang.malik@anu.edu.au (UM); rob.sharp@anu.edu.au (RS)

in order to ensure the light-curve variability and reverberation lag are resolved (Horne et al. 2004). Early surveys monitored AGN on a source-by-source basis, making observations over several months to years. Lag measurements were made for dozens of sources, using the Hβ line (e.g. Peterson et al. 1998; Kaspi et al. 2000; Peterson & Horne 2004; Bentz et al. 2009). From these measurements, a tight correlation was found between the AGN luminosity and the radius of the BLR (*R–L* relation; e.g. Bentz et al. 2009, 2013). Lags recovered using higher ionization emission lines (e.g. C IV) were found to be shorter than lags recovered using lower ionization emission lines (e.g. Hβ), demonstrating the ionization stratification of the BLR (Gaskell & Sparke 1986; Dietrich et al. 1993). The *R–L* relation is importantly used to calibrate secondary mass-scaling relations to estimate single-epoch virial BH masses (e.g. Shen et al. 2011), and has also been proposed as a way to standardize AGN for use as a cosmological distance indicators (Watson et al. 2011; Martínez-Aldama et al. 2019).

Through the advent of wide-field photometric surveys such as the Dark Energy Survey, (DES; Dark Energy Survey Collaboration et al. 2016), multi-epoch photometric data for large samples of AGN has become readily available. Concurrent observations can be made with multi-object spectrographs; however, the demand for these instruments is high and therefore limits the number of epochs that can be feasibly acquired. The Australian Dark Energy Survey (OzDES) and Sloan Digital Sky Survey Reverberation Mapping (SDSS-RM) Project have conducted the first multi-object RM surveys, observing hundreds of AGN probing a wide range of AGN luminosities and redshifts (King et al. 2015; Shen et al. 2015). These programs have delivered over one hundred new lag measurements (Grier et al. 2017; Grier et al. 2019; Hoormann et al. 2019; Homayouni et al. 2020; Yu et al. 2021; Malik et al. 2023; Yu et al. 2023, Penton et al. in prep). This allowed the Mg II and C IV *R– L* relations to be constrained for the first time using statistically significant samples; however, there is significant scatter in the measurements. This is mostly due to challenges with data quality (low signal to noise, limited sampling; see Malik et al. 2022) and lag recovery reliability (Li et al. 2019; Penton et al. 2022). These factors have limited the lag recovery efficacy of each survey to about 10–25 per cent.

Stacking can be used to combine the cross-correlation signals of physically similar AGN to recover average lags for these objects. The technique was first applied by Fine et al. (2012, 2013) using only two spectroscopic epochs, which yielded a marginal result. After demonstrating the success of the technique with the Bentz et al. (2013) Hβ sample, Li et al. (2017) measured composite lags with Hα, Hβ, He II, and Mg II using a subset of the SDSS-RM sample. Stacked averages are not swayed by the systematic errors from individual sources. Their consistency (or not) with the measurements made for individual sources is therefore important. Additionally, with the wide redshift range covered by our sample, the gaps in the observational window function can be filled in to some extent. Therefore, stacking leverages the data in a way that cannot be done with traditional individual measurements.

We present a stacked lag analysis of the entire OzDES sample, for the Hβ, Mg II, and C IV lines. Section 2 details the observations obtained by OzDES and the data calibration procedures. In Section 3, we describe the technique used to recover stacked lags. In Section 4, we present our average lag measurements, and comparisons with individual measurements on the respective *R– L* relationships for each emission line. We summarize our results and the discuss the outlook to the future in Section 5.

Throughout this work we adopt a flat ΛCDM cosmology, with $\Omega_\Lambda = 0.7$, $\Omega_M = 0.3$, and $H_0 = 70 \text{ km s}^{-1} \text{ Mpc}^{-1}$.
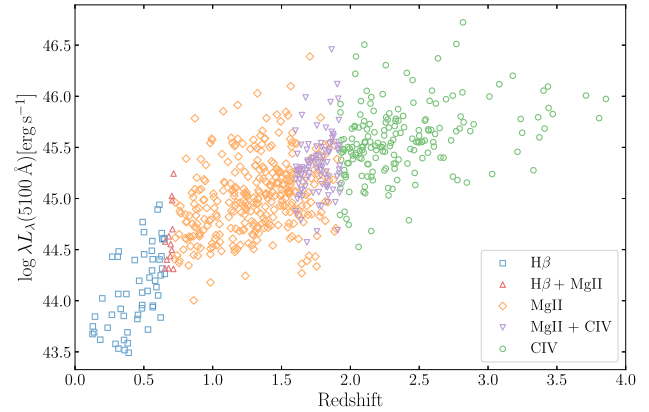
Figure 1. Distribution of redshifts and monochromatic luminosity at 5100 Å for the 690 AGN in the OzDES RM sample. The Hβ sample extends to $z = 0.75$, with 13 sources overlapping with our Mg II sample. The Mg II sample extends to $z = 1.92$, with 106 sources overlapping with our C IV sample.

2 DATA

Our photometric data were obtained as part of the Dark Energy Survey (DES) Supernova Program, which observed 10 deep fields covering 27 deg^2, comprising the ELAIS, *XMM–LSS*, *Chandra* deep-field South, and SDSS Stripe 82 fields (Kessler et al. 2015; Morganson et al. 2018). These fields were observed in the *griz* filters, with the Dark Energy Camera (DECam) on the 4-m Blanco telescope at Cerro Tololo Inter-American Observatory (CTIO; Flaugher et al. 2015). The fields were observed with ~6 d cadence over a 5–6 month season (August to January) from 2013 to 2018, with additional science verification data taken in 2012. The OzDES project (Yuan et al. 2015; Childress et al. 2017; Lidman et al. 2020) conducted follow-up spectroscopic observations with the 2dF multi-object fibre positioning system and the AAOmega spectrograph (3700–8800 Å, Sharp et al. 2006) on the 3.9-m Anglo-Australian Telescope (AAT), taken with approximately monthly cadence over the same seasons, from 2013 to 2019. After the conclusion of the Supernova Program, additional DECam observations were taken monthly in the 2018–19 season, taking the baseline of our photometric light curves to 7 years.

The OzDES Reverberation Mapping sample comprises 735 AGN, ranging from 0.1 < z < 4.0, with apparent magnitudes 17.2 < r_{AB} < 22.3 (Tie et al. 2017). Of these 735 AGN, we removed 9 of the 78 AGN from the Hβ sample due to broad-absorption lines (BALs) or incorrect classification as a Type 1 AGN, 3 of the 453 AGN from the Mg II sample for the same reason (these sources overlapped with the Hβ sample), and 88 of the 378 AGN from the C IV sample due to BALs. These sources were included in the initial survey selection to improve the source density in the sky and study BAL variability, but have proven challenging for reverberation analysis. The final sample we use in this analysis comprises 69 Hβ sources, 450 Mg II sources, and 290 C IV sources (690 AGN in total). The redshift and luminosity distribution of these targets is shown in Fig. 1.

As done for the individual lag measurements made by Yu et al. (2023) and Malik et al. (2023), for the Hβ and Mg II samples, we measure the emission-line flux from spectra obtained on different nights as separate epochs in order to maximize the cadence of our sampling for our emission-line light curves. As we have lower signal to noise for the C IV sample, we co-add the spectra over each

observing run (typically 4–7 nights during dark time each month), as done by Hoormann et al. (2019).

We do not measure the continuum luminosity directly from the spectra due to fibre aperture effects from variable atmospheric seeing and fibre placement uncertainties. From the average *r*-band magnitude and redshift of the AGN, we estimated the monochromatic continuum flux at rest frame 5100, 3000, and 1350 Å, using the DECam *r*-band filter transmission curve and the SDSS quasar template (Vanden Berk et al. 2001). The template is scaled to the magnitude of the source, assuming $L_{bol} = 9\,\lambda L_\lambda\,(5100\,\text{Å})$ (Kaspi et al. 2000). The source properties for the OzDES sample used in this work are provided in Section A, and complete sample characteristics for the final OzDES RM sample will be provided in a future OzDES RM Program paper.

The DES photometry is calibrated using the DES data reduction pipeline (Burke et al. 2018; Morganson et al. 2018). We perform a spectrophotometric flux calibration following Hoormann et al. (2019). For the Hβ and C IV samples, we measure the line fluxes as done by Hoormann et al. (2019). For the continuum subtraction, the local continuum windows we use for Hβ are 4760 to 4790 Å and 5100 to 5130 Å, and for C IV are 1450 to 1460 Å and 1780 to 1790 Å. For the Mg II sample, the iron subtraction and line flux measurement is performed as detailed in Yu et al. (2023). The calibration uncertainties of the line flux for each line are measured using the F-star warping function method as detailed in Yu et al. (2021).

3 LAG RECOVERY METHOD

As reverberation lags should be dependent on the intrinsic AGN luminosity alone (at least to first order), we bin the sources by their continuum luminosity. Further details are provided for each emission-line subsample in Section 4.

For each source in a redshift-luminosity bin, we covert the observation dates to the rest frame of the source by dividing by $(1 + z)$. We use the PyCCF code to perform the interpolated cross-correlation function method for each individual source (ICCF; Gaskell & Peterson 1987; Sun, Grier & Peterson 2018). The continuum and emission-line light curves of each source are linearly interpolated to a grid spacing of 3 d. The interpolated light curves are cross-correlated as a function of time-lag. We then average the cross-correlation functions (CCF) of each source in the bin to obtain the stacked CCF. We search for lags over a (rest-frame) lag range of [−100, 300] d for Hβ and C IV, and [−100, 500] d for Mg II as it has a longer expected lag for our sample.

We measure the average lag and its uncertainties by bootstrapping the sample in each bin. We perform the above procedure to calculate the stacked CCF's for each bootstrapped re-sample of the original binned sample. We repeat this 1000 times, and record the centroid of each CCF (r_{max}) to build the bootstrap distribution, from which we adopt the median and 16th and 84th percentiles of this distribution as the recovered average stacked lag, τ, and lower and upper uncertainties, σ_τ, for the bin.

Following Li et al. (2017), we shuffle the spectroscopic epochs and repeat the stacking for 100 Monte Carlo realizations, and compare the stacked CCF produced by these uncorrelated light curves to the original stacked CCF. This is similar to the null hypothesis test used by Malik et al. (2023) to check that the lag recovery is not simply a product of the interaction of the window function with underlying red-noise correlation in the photometric light curves, considering the relatively low sampling density and modest signal to noise of our light curves.
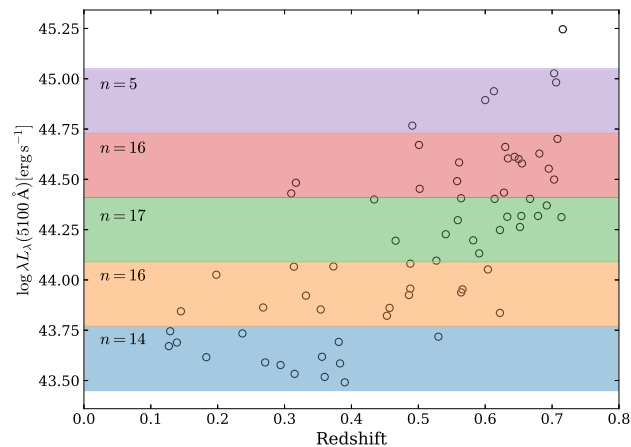

Figure 2. The luminosity bins for the Hβ sample, labelled with the number of binned sources. Within each bin, the standard deviation of the expected lags for the individual sources (measured using the source luminosity and the Bentz et al. (2013) *R*–*L* relation for Hβ) is ∼10 per cent of the expected mean lag for the binned sample (measured as the mean of the expected lags for the individual sources).

4 RESULTS

We present the results of our stacking analysis for each emission line sample in the OzDES RM sample, and a multiline analysis of the subsamples for which two emission-lines are present. With the basic assumption that the lag of a source is dependent on the intrinsic AGN luminosity alone, by using the stacking method, we are assuming the lags of each source within a bin are similar (in the rest-frame) so that we recover a representative average lag for these AGN. Since the binned sources are at different redshifts, when the light curve data is converted to the rest-frame, different variability and reverberation time-scales are probed by each source through their unique rest-frame observational window function. By stacking, we can partially circumvent the usual impact of the sparse sampling (particularly the 7-month seasonal gaps) in the light curves of any one source, as we are combining the CCF's for all sources in a bin. We compare the average lag measurements to the sample of existing individual lag measurements on the respective *R*–*L* relations for each line.

4.1 Hβ

We divide our sample into five luminosity bins of equal size, as shown in Fig. 2. The size of the bins were chosen as to maximize the number of sources in each bin while avoiding introducing a broad underlying distribution in the expected lags. The highest luminosity source was excluded from the analysis for this reason. Although there are a relatively small number of sources stacked in each bin, particularly when compared to stacking done by Fine et al. (2012, 2013), the signal to noise of our stacked CCF's are sufficiently high as we have much more light curve data.

The stacked CCF's for each bin of the Hβ sample are shown in Fig. 3, alongside the total number of overlapping light curve epochs as a function of time-lag for all sources stacked within the bin. As the observation dates of each source in a bin are converted to the rest-frame of the source, and there is a distribution of source redshifts within each bin, the total light curve sampling of the stacked sample begins to in-fill the rest frame observational gap imposed by the observed frame 7-month seasonal gap present in the individual observed light curves.
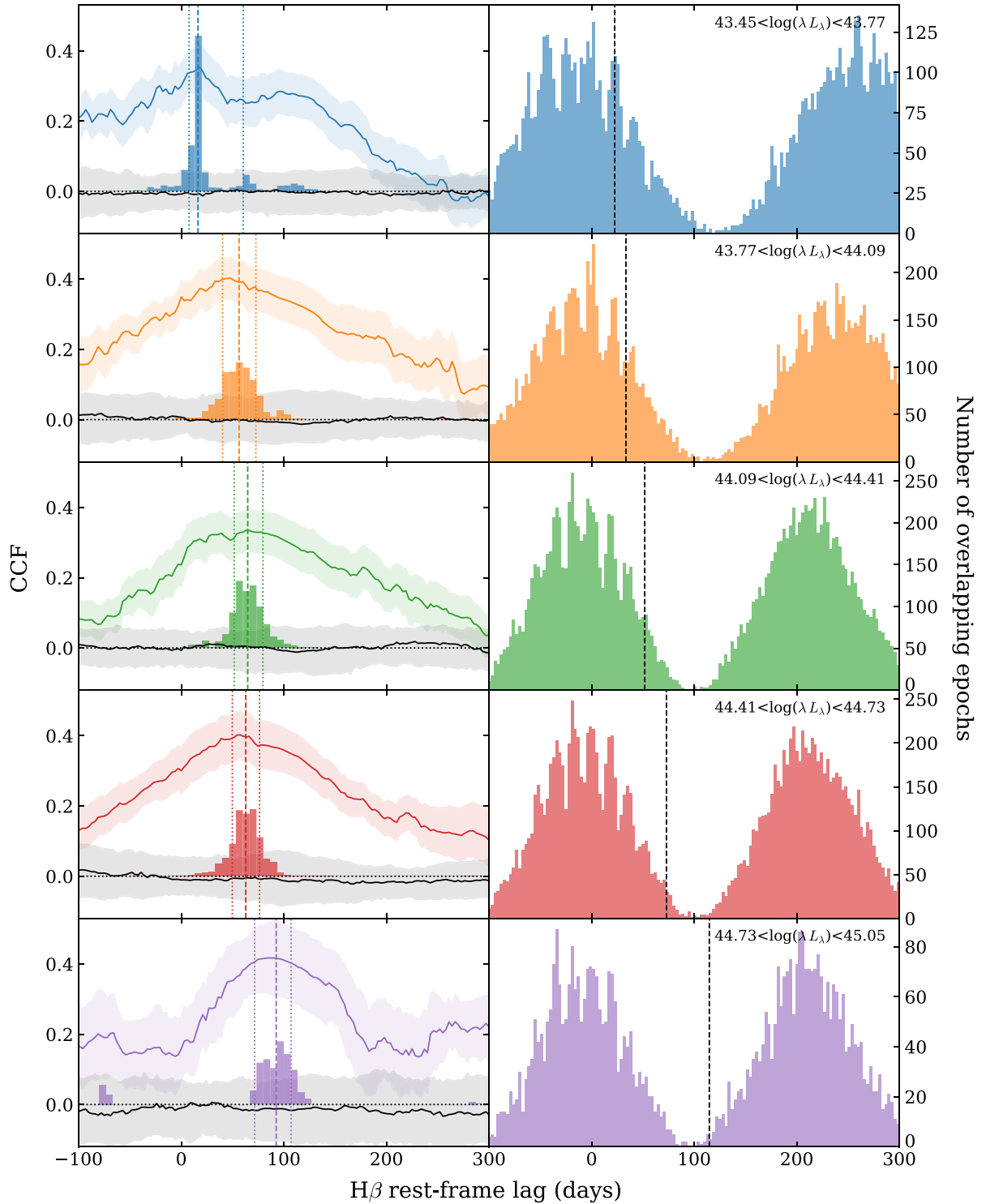
Figure 3. *Left column:* The coloured solid lines are the stacked cross correlation functions (CCF) for each of the five luminosity bins for the Hβ sample. The colours correspond to the respective bins in Fig. 2. The 1σ scatter of the bootstrapped CCF's is shown by the coloured shaded region. The vertical dashed and dotted lines indicate the recovered average lag and its uncertainty, as measured from the bootstrap distribution (coloured histogram). The black solid line and grey shaded area show the mean and 1σ scatter of the CCF's generated using the randomized spectroscopic light curves following the procedure described in Section 3. *Right column:* The number of overlapping spectroscopic and photometric epochs as a function of time lag, in total, for each source in the corresponding bin. The expected mean lag for the bin is indicated by the black dashed line.
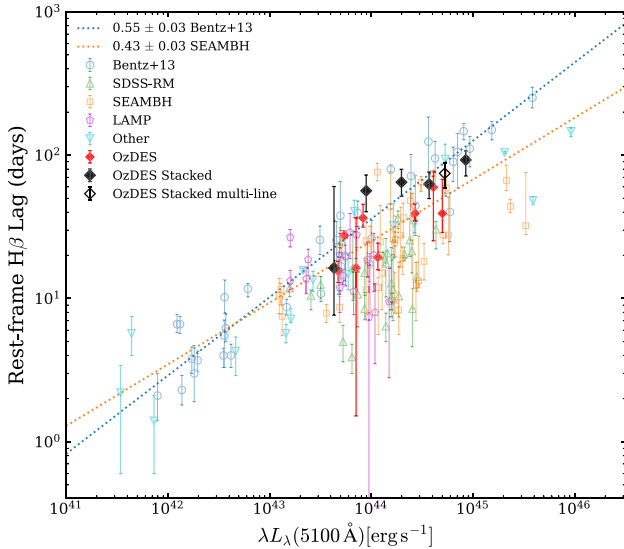
Figure 4. The Radius–Luminosity relation for Hβ (dotted lines), including the stacked average lag measurements made using the OzDES Hβ sample, and existing individual lag measurements from Bentz et al. (2013, and references therein); SDSS-RM (Grier et al. 2017, quality 4 and 5); SEAMBH (Du et al. 2014; Wang et al. 2014; Du et al. 2015, 2016, 2018; Hu et al. 2021); Lick AGN Monitoring Project (LAMP, U et al. 2022); and other measurements from Bentz et al. (2009); Barth et al. (2013); Bentz et al. (2014); Pei et al. (2014); Lu et al. (2016); Bentz et al. (2016a, b); Fausnaugh et al. (2017); Rakshit et al. (2019); Zhang et al. (2019); Li et al. (2021), of which measurements published before 2019 are compiled by Martínez-Aldama et al. (2019). The multiline average lag measurement is presented in Section 4.4.

Comparing the stacked CCF, and its scatter measured from bootstrapping, to the stacked CCF's after light curve randomization, we see significant correlation signal present. This implies that the signal is not dominated by the correlation of any individual source. In all cases, there is one major peak present; however, the lowest luminosity bin (blue) has a flatter CCF. There is limited but non-zero data overlap around the expected mean lags for the two highest luminosity bins, as they coincide with the first seasonal gap in our light curves. However, we recover significant average lags in each of these bins. This demonstrates the ability of stacking to overcome the limitations imposed by sparse sampling, which impede lag recovery for individual sources.

We plot the recovered average lags from each luminosity bin on the *R–L* relation, as shown in Fig. 4. Our stacked measurements are consistent with the Bentz et al. (2013) slope, which agrees with the physically motivated slope of ∼0.5. The uncertainty in the average lags is consistent to the uncertainties in the eight lags recovered for individual sources (Malik et al. 2023), and is inconsistent with the distribution of the SDSS-RM measurements (Grier et al. 2017; Li et al. 2017), for which shorter lags are recovered. Given the similarities of our programs and sample selection, the reason for this discrepancy is unclear. Although the main difference between the surveys is the baseline and cadence of the data, simulations by Fonseca Alvarez et al. (2020) and Malik et al. (2022) find that this does not bias the lag recovery of SDSS-RM to shorter lags, or OzDES to longer lags. For our composite lags, we bin across our entire Hβ sample, and do not reject any sources based on light curve signal to noise, or any other criteria.

As a test, we repeated the stacking after excluding all the objects with individual recovered lags (Malik et al. 2023). We show the
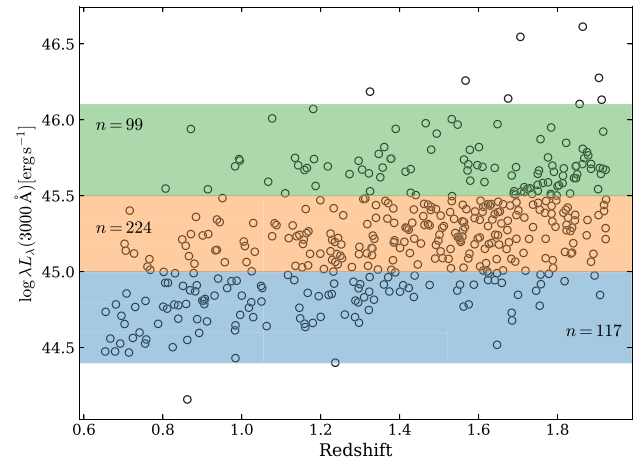

Figure 5. The luminosity bins for the Mg II sample, labelled with the number of binned sources. Within each bin, the standard deviation of the expected lags for the individual sources (measured using the source luminosity and the Trakhtenbrot & Netzer (2012) *R–L* relation for Mg II) is ∼20 per cent of the expected mean lag for the binned sample.

results of this test in Section B. Although the average lag uncertainties increase after the exclusion, the lags remain in close agreement with those from the original analysis.

4.2 Mg II

The three luminosity bins used for the Mg II sample are shown in Fig. 5. The lowest and highest luminosity bins are slightly wider to include sources close to the edge of the bin. Ten sources were excluded from the analysis to optimize the bin densities and reduced smoothing of the stacked CCF's. Larger luminosity bins were required to achieve adequate signal to noise in the stacked CCF's for this sample.

We present the stacked CCF's in Fig. 6. The strength of the correlation signals in each bin is lower than for the Hβ sample; however, comparing to the CCF's produced using randomized light curves, we can see there is significant signal present. The signal to noise of the Mg II light-curve input data is lower than for the Hβ sample, as the Mg II sample is fainter and requires subtraction of Fe II from the emission-line (Yu et al. 2021, 2023). However, we have 450 AGN in the Mg II sample, and are therefore stacking many more sources in each bin. Since sample size is not the limiting factor in this case, the lower signal to noise of the Mg II line light curves must be producing weaker stacked cross correlation signals. In the lowest luminosity bin, the signal is flat and no clear peak is present. For the other two bins, a dominant peak is present, and the bootstrap distributions are adequately constrained to recover average lags.

We plot the recovered average lags from each luminosity bin on the Mg II *R–L* relation in Fig. 7, along with the 25 individual measurements made with this sample by Yu et al. (2023). The average lags are in agreement with the recent individual measurements from Homayouni et al. (2020) and Yu et al. (2023). There is no clear progression to longer lags with higher luminosities given that the average lags for the lowest and intermediate luminosity bins are not particularly well constrained. As shown in Fig. 6, there is limited data coverage over the expected mean lags for the lowest luminosity bin (blue), which coincides with the first seasonal gap in our light curves. The time-dilation distribution over the binned sample is not sufficient to 'fill in' the short time-scales, but it is able to
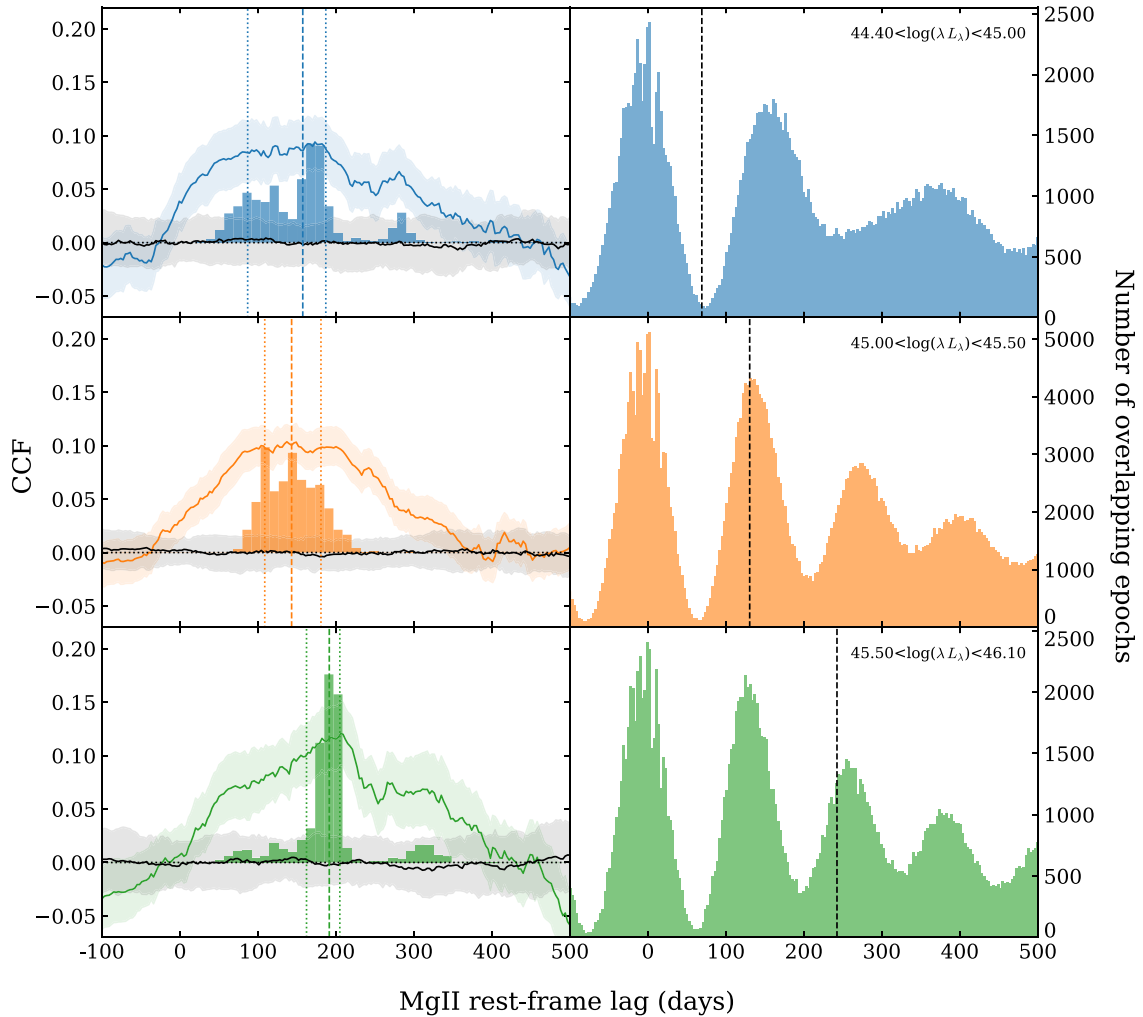
Figure 6. *Left column:* The coloured solid lines are the stacked cross correlation functions (CCF) for each of the three luminosity bins for the Mg II sample. The colours correspond to the respective bins in Fig. 5. The 1σ scatter of the bootstrapped CCF's is shown by the coloured, shaded region. The vertical dashed and dotted lines indicate the recovered average lag and its uncertainty, as measured from the bootstrap distribution (coloured histogram). The black solid line and grey shaded area show the mean and 1σ scatter of the CCF's generated using the randomized spectroscopic light curves following the procedure described in the text. *Right column:* The number of overlapping spectroscopic and photometric epochs as a function of time lag, in total, for each source in the corresponding bin. The expected mean lag for the bin is indicated by the black dashed line.

sufficiently bridge the second seasonal gap. This could explain why the uncertainty on the recovered average lag for the lowest luminosity bin is larger than the uncertainties for the intermediate and highest luminosity bins. The average lags for the three luminosity bins are formally consistent with both the steeper *R–L* relation measured by Trakhtenbrot & Netzer (2012), and the shallower relation recently constrained by Yu et al. (2023), however, the better constrained mean lag for the highest luminosity bin is only consistent with the shallower relation.

4.3 C IV

As for the previous samples, we present the luminosity bins for the C IV sample in Fig. 8, and the stacked CCF results in Fig. 9. As required for Mg II, larger luminosity bins were necessary to achieve sufficient signal to noise after stacking, and nine sources were excluded from the analysis to avoid overly wide bins in luminosity. The OzDES C IV sample has lower signal to noise than the Hβ and

Mg II samples, as the AGN are faint. The bootstrap distributions are not well constrained for the lowest or highest luminosity bins. However, Li et al. (2017) found that the mean recovered lag remains stable when the light curve signal to noise is degraded, although the uncertainty increases proportionally with the decline. Therefore, we continue to recover the average lags and compare with individual source measurements.

We plot the stacked average lags from the C IV sample alongside existing measurements from the literature in Fig. 10. The average lags for the intermediate and highest luminosity bins are in agreement with the *R–L* relations constrained by Hoormann et al. (2019) and Grier et al. (2019), although the uncertainty on the average lag for the highest luminosity bin is large. As discussed for the Mg II sample, the time dilation over the binned samples does not sufficiently bridge the first of the 7-month seasonal gaps in our light curves. With the shorter expected lags for C IV, the average lags for the lowest and intermediate luminosity bins coincides with this gap. In addition to the lower signal to noise of the light curves, this may be contributing
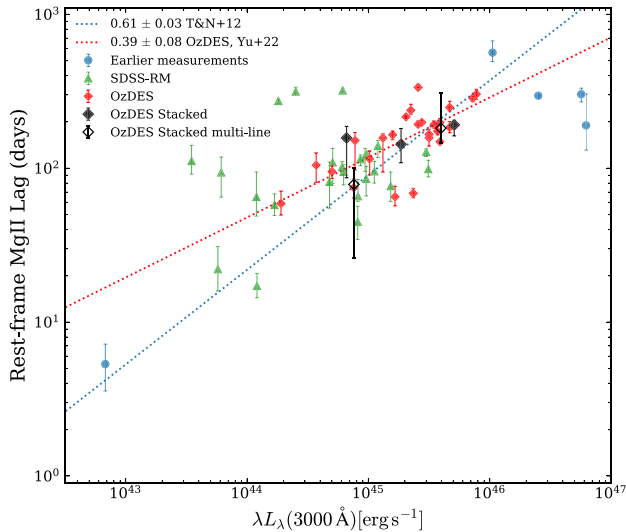
Figure 7. Radius–Luminosity relation for Mg II, with existing individual lag measurements from Metzroth, Onken & Peterson (2006); Lira et al. (2018); Czerny et al. (2019); Zajaček et al. (2020, 2021) and SDSS-RM (Homayouni et al. 2020, gold sample), along with the OzDES individual measurements (Yu et al. 2023), and our stacked average lag measurements. The multiline average lag measurements are presented in Section 4.4.
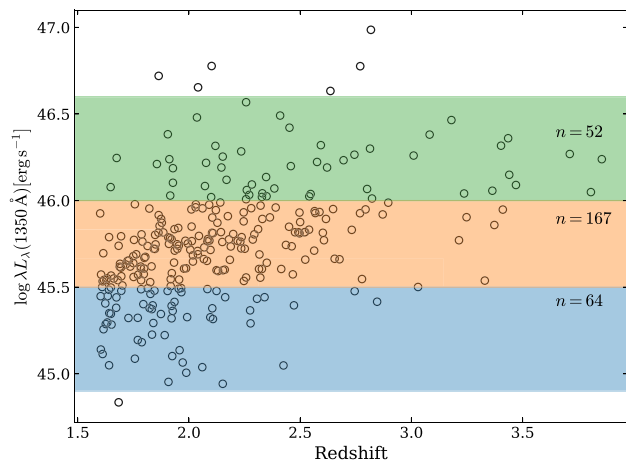

Figure 8. The luminosity bins for the C IV sample, labelled with the number of binned sources. Within each bin, the standard deviation of the expected lags for the individual sources (measured using the source luminosity and the Hoormann et al. (2019) R–L relation for C IV) is ∼15 per cent of the expected mean lag for the binned sample.

to the poorer quality of the stacked CCF's. It is unclear why the average lag recovered for the lowest luminosity bin is much longer than expected.

4.4 Multiline measurements

Both the Hβ and Mg II lines are visible for 13 AGN, and Mg II and C IV for 106 AGN (see Fig. 1). We attempt to recover average lags independently with each line, in order to compare the lag ratios to investigate the ionization stratification of the BLR.

We repeated the stacking procedure for the sample of 13 AGN with the Hβ and Mg II light curves. As there are few sources we do not bin them by luminosity. We present the stacked CCF's for

each line in Fig. 11. We measure an average lag of 75^{+14}_{-16} d for the Hβ sample, and an average lag of 79^{+22}_{-53} d for the Mg II sample. We formally recover a Mg II to Hβ lag ratio of 1.05 ± 0.54; however, the inherent uncertainty is significant due to the large uncertainty of the Mg II average lag. This result is broadly consistent with the expectation that these two BLRs are approximately cospatial. This ratio is consistent with previous multiline measurements made by Homayouni et al. (2020), who found that Mg II is emitted from a similar or slightly larger region than Hβ in several individual sources, as well as Clavel et al. (1991) and Czerny et al. (2019).

We repeated this for the sample of 106 AGN with Mg II and C IV, and present the stacked CCF's in Fig. 12. The signal to noise was insufficient to divide the sample into two luminosity bins. We measure an average Mg II lag of 182^{+128}_{-37} d, and an average C IV lag of 64^{+165}_{-45} d. We formally recover a Mg II to C IV lag ratio of 2.84 ± 4.84; however, this is poorly (if at all) constrained given that the average lags are not well constrained (particularly for the CIV sample). The average lags are broadly consistent with the BLR stratification model, and the multiline comparison made for a single source by Homayouni et al. (2020).

We include the average lags recovered from the multiline samples on the respective R–L plots presented in Figs 4, 7, and 10. We also provide all average lags recovered in this work from each multiline and emission line sample in Table 1.

5 SUMMARY

We use the stacking technique developed by Fine et al. (2012, 2013) to measure average lags in luminosity bins for the Hβ, Mg II, and C IV samples from the OzDES Reverberation Mapping Program. By utilizing the bulk of our sample to recover composite lags, we avoid the potential selection biases in the lag recovery for individual sources. We successfully recover significant cross-correlation signals for each emission-line sample:

(i) The average lags from each luminosity bin of the Hβ sample are consistent with the R–L relation constrained by Bentz et al. (2013), and the size of the uncertainties on the average lags are on par with that of individual measurements, despite the relatively small number of sources stacked in each bin. This provides confidence in the individual measurements, and demonstrates the potential for stacked RM analyses to improve upon constraints that have thus far been made with individual source measurements alone.

(ii) For Mg II and C IV, the stacked cross-correlations are weaker, but still present above the correlation signal generated using randomized light curves. Further data or larger samples are required to recover significant average lags for these samples across each luminosity bin.

(iii) From our multiline analysis, we measure a Mg II to Hβ lag ratio that is consistent with earlier findings that the size of each of these line-emitting regions is similar. Our average lags for the Mg II and C IV multiline samples are not well-constrained due to the limited sample size; however, the lag ratio we recover is largely consistent with the BLR ionization stratification model.

Stacking can be applied beyond RM-specific surveys. It can be done with just a few spectroscopic epochs, using large AGN samples, provided the continuum behaviour is well sampled. With LSST forthcoming, high cadence photometry of the deep-drilling fields will yield quality continuum light curves for tens of thousands of AGN. The SDSS-V Black Hole Mapper (BHM) will be spectroscopically following these fields. In addition to their dedicated RM survey of ∼1000 AGN, SDSS-V BHM will monitor 25 000 AGN over
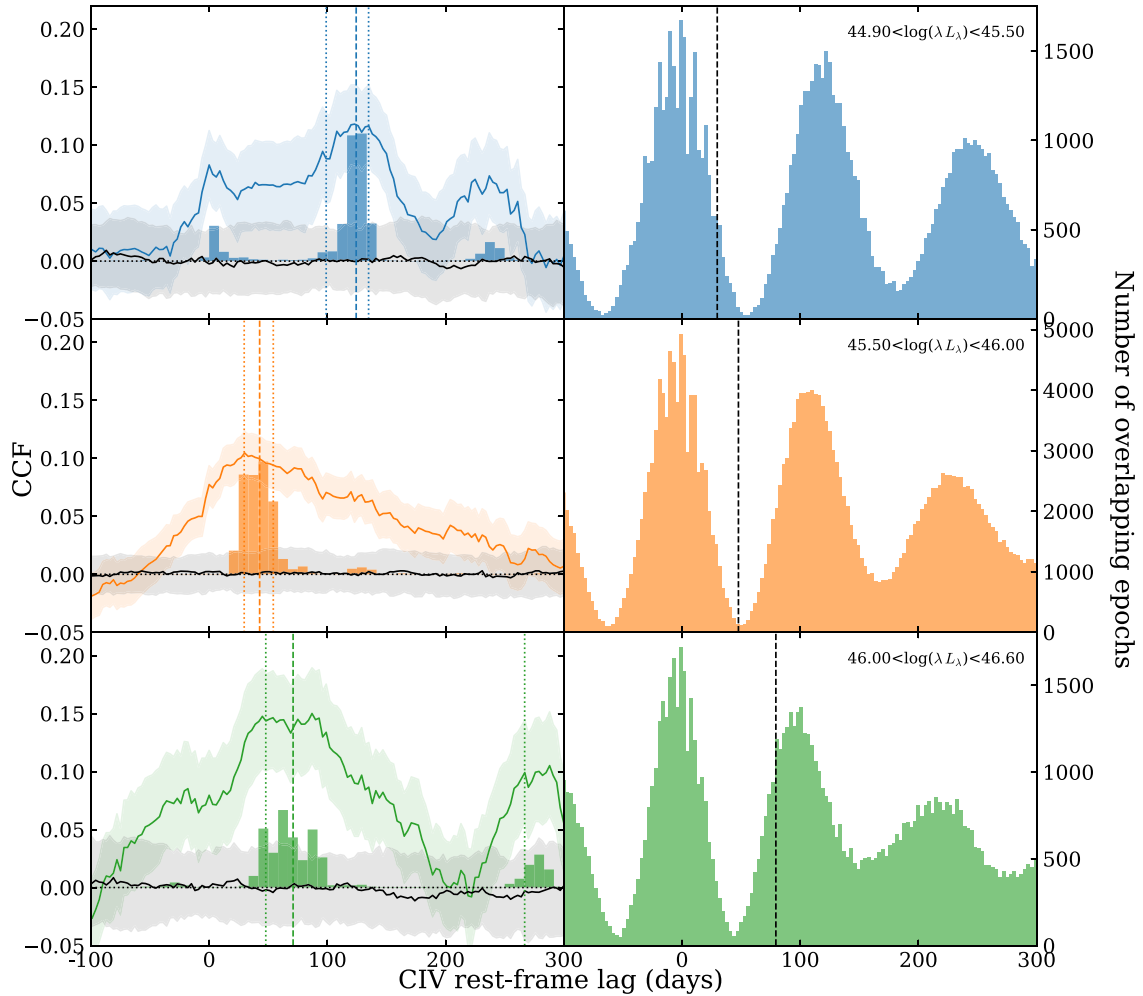
Figure 9. *Left column:* The coloured solid lines are the stacked cross correlation functions (CCF) for each of the three luminosity bins for the C IV sample. The colours correspond to the respective bins in Fig. 8. The 1σ scatter of the bootstrapped CCF's is shown by the coloured shaded region. The vertical dashed and dotted lines indicate the recovered average lag and its uncertainty, as measured from the bootstrap distribution (coloured histogram). The black solid line and grey shaded area show the mean and 1σ scatter of the CCF's generated using the randomized spectroscopic light curves following the procedure described in the text. *Right column:* The number of overlapping spectroscopic and photometric epochs as a function of time lag, in total, for each source in the corresponding bin. The expected mean lag for the bin is indicated by the black dashed line.

multiple epochs, which will be combined with earlier SDSS spectra (Kollmeier et al. 2017). The Time Domain Extragalactic Survey (TiDES) will also be following up these fields to conduct an RM survey of ~ 700 AGN up to $z \sim 2.5$ (Swann et al. 2019). Stacking analyses of these future, large samples have promise to significantly extend the reverberation mapping results from these projects. Although the improved signal to noise and survey sampling of these future programs are expected to yield an increased number of

higher quality individual lag measurements than the first generation of multi-object RM surveys, these data sets can benefit from the ability of stacking to alleviate the impact of the unavoidable seasonal gaps on lag recovery (Malik et al. 2022). Stacking also presents an opportunity to combine all large time-domain data sets to recover average lags that are potentially more robust than individual lags, which remain challenging to recover reliably, particularly at high redshift.
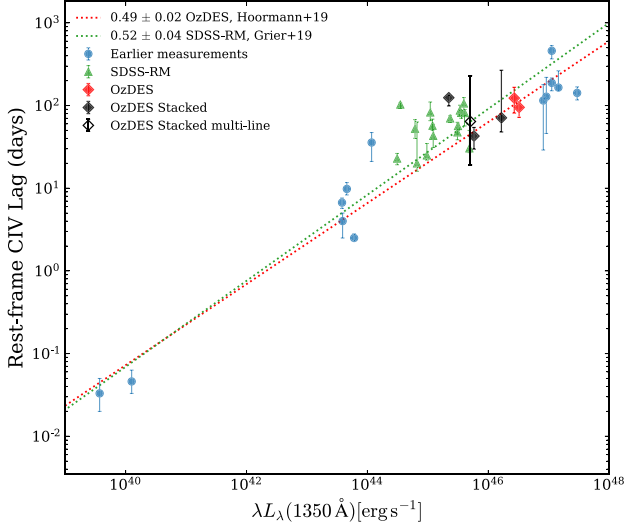
Figure 10. Radius–Luminosity relation for C IV, with our stacked average lags and existing individual lag measurements from Peterson et al. (2005, and references therein); Kaspi et al. (2007); Trevese et al. (2014); Lira et al. (2018), and SDSS-RM (Grier et al. 2019; Shen et al. 2019, gold sample), Kaspi et al. (2021), along with the OzDES individual measurements (Hoormann et al. 2019). The multiline average lag measurement is presented in Section 4.4.
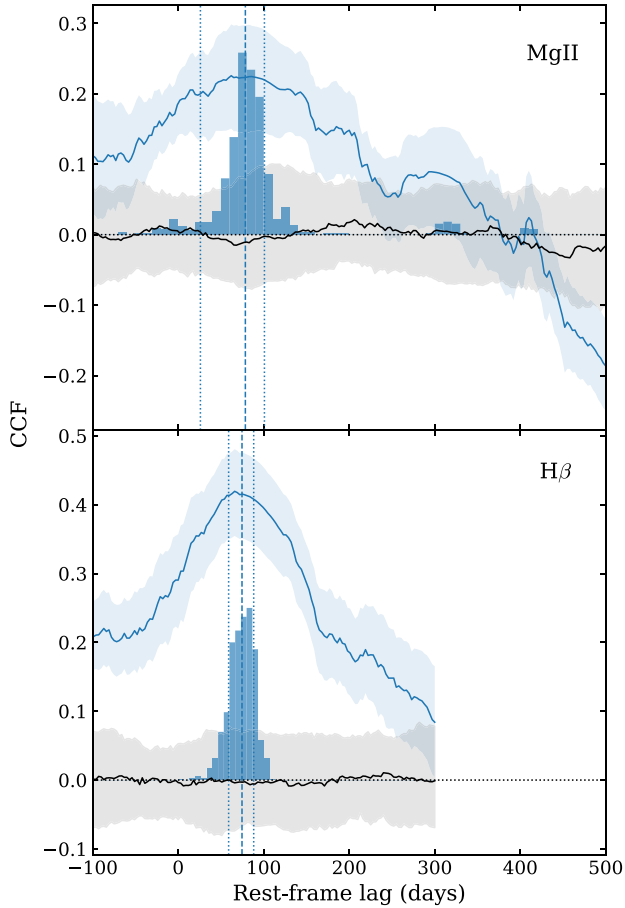
Figure 11. The stacked cross correlation functions (CCF) for the multiline sample with both Hβ and Mg II, comprising 13 AGN.
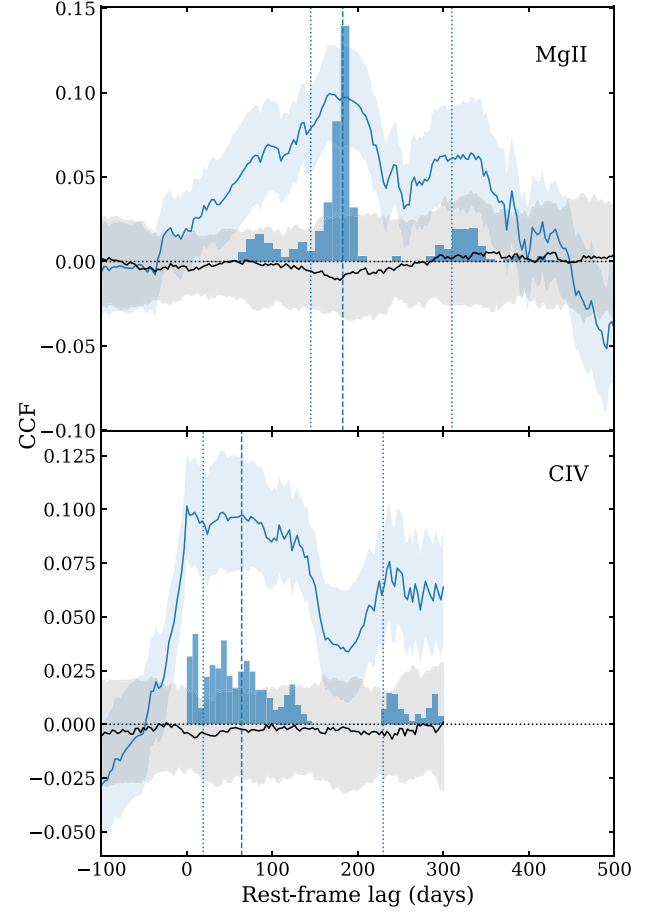
Figure 12. The stacked cross correlation functions (CCF) for the multiline sample with both Mg II and C IV, comprising 106 AGN.

Table 1. The average lags for each luminosity bin or multiline sample, for each emission-line sample from the OzDES RM Program. Luminosities are given in erg s^{-1}, and average lags are in the rest frame.

Hβ	
Binned sample	Average lag (d)
$43.45 < \log(\lambda L_\lambda) < 43.77$	16^{+44}_{-9}
$43.77 < \log(\lambda L_\lambda) < 44.09$	56^{+16}_{-16}
$44.09 < \log(\lambda L_\lambda) < 44.41$	65^{+15}_{-13}
$44.41 < \log(\lambda L_\lambda) < 44.73$	63^{+13}_{-13}
$44.73 < \log(\lambda L_\lambda) < 45.05$	93^{+14}_{-21}
multiline Hβ + Mg II	75^{+14}_{-16}
Mg II	
Binned sample	Average lag (d)
$44.40 < \log(\lambda L_\lambda) < 45.00$	157^{+30}_{-71}
$45.00 < \log(\lambda L_\lambda) < 45.50$	143^{+38}_{-34}
$45.50 < \log(\lambda L_\lambda) < 46.10$	191^{+14}_{-29}
multiline Mg II + Hβ	79^{+22}_{-53}
multiline Mg II + C IV	182^{+128}_{-37}
C IV	
Binned sample	Average lag (d)
$44.90 < \log(\lambda L_\lambda) < 45.50$	124^{+11}_{-25}
$45.50 < \log(\lambda L_\lambda) < 46.00$	43^{+12}_{-13}
$46.00 < \log(\lambda L_\lambda) < 46.60$	71^{+196}_{-23}
multiline C IV + Mg II	64^{+165}_{-45}

DATA AVAILABILITY

The underlying DES and OzDES data are available in Abbott et al. (2021) and Lidman et al. (2020). The final light curve data for the full OzDES RM data set will be made available in a future OzDES paper.

REFERENCES

Abbott T. M. C. et al., 2021, ApJS, 255, 20
Astropy Collaboration et al., 2013, A&A, 558, A33
Astropy Collaboration et al., 2018, AJ, 156, 123
Barth A. J. et al., 2013, ApJ, 769, 128
Bentz M. C., Peterson B. M., Netzer H., Pogge R. W., Vestergaard M., 2009, ApJ, 697, 160
Bentz M. C. et al., 2013, ApJ, 767, 149
Bentz M. C. et al., 2014, ApJ, 796, 8
Bentz M. C., Cackett E. M., Crenshaw D. M., Horne K., Street R., Ou-Yang B., 2016a, ApJ, 830, 136
Bentz M. C. et al., 2016b, ApJ, 831, 2
Blandford R. D., McKee C. F., 1982, ApJ, 255, 419
Burke D. L. et al., 2018, AJ, 155, 41
Childress M. J. et al., 2017, MNRAS, 472, 273
Clavel J. et al., 1991, ApJ, 366, 64
Czerny B. et al., 2019, ApJ, 880, 46
Dark Energy Survey Collaboration et al., 2016, MNRAS, 460, 1270
Dietrich M. et al., 1993, ApJ, 408, 416
Du P. et al., 2014, ApJ, 782, 45
Du P. et al., 2015, ApJ, 806, 22
Du P. et al., 2016, ApJ, 825, 126
Du P. et al., 2018, ApJ, 856, 6
Event Horizon Telescope Collaboration et al., 2019, ApJ, 875, L6
Fausnaugh M. M. et al., 2017, ApJ, 840, 97
Fine S. et al., 2012, MNRAS, 427, 2701
Fine S. et al., 2013, MNRAS, 434, L16
Flaugher B. et al., 2015, AJ, 150, 150
Fonseca Alvarez G. et al., 2020, ApJ, 899, 73
Gaskell C. M., Peterson B. M., 1987, ApJS, 65, 1
Gaskell C. M., Sparke L. S., 1986, ApJ, 305, 175
Gebhardt K. et al., 2000, ApJ, 543, L5
Gebhardt K., Adams J., Richstone D., Lauer T. R., Faber S. M., Gültekin K., Murphy J., Tremaine S., 2011, ApJ, 729, 119
Grier C. J. et al., 2017, ApJ, 851, 21
Grier C. J. et al., 2019, ApJ, 887, 38
Harris C. R. et al., 2020, Nature, 585, 357
Homayouni Y. et al., 2020, ApJ, 901, 55
Hoormann J. K. et al., 2019, MNRAS, 487, 3650
Horne K., Peterson B. M., Collier S. J., Netzer H., 2004, PASP, 116, 465
Hu C. et al., 2021, ApJS, 253, 20

Hunter J. D., 2007, Comput. Sci. Eng., 9, 90

Kaspi S., Smith P. S., Netzer H., Maoz D., Jannuzi B. T., Giveon U., 2000, ApJ, 533, 631

Kaspi S., Brandt W. N., Maoz D., Netzer H., Schneider D. P., Shemmer O., 2007, ApJ, 659, 997

Kaspi S., Brandt W. N., Maoz D., Netzer H., Schneider D. P., Shemmer O., Grier C. J., 2021, ApJ, 915, 129

Kessler R. et al., 2015, AJ, 150, 172

King A. L. et al., 2015, MNRAS, 453, 1701

Kollmeier J. A. et al., 2017, preprint (arXiv:1711.03234)

Kuo C. Y. et al., 2011, ApJ, 727, 20

Li J. et al., 2017, ApJ, 846, 79

Li J. I.-H. et al., 2019, ApJ, 884, 119

Li S.-S. et al., 2021, ApJ, 920, 9

Lidman C. et al., 2020, MNRAS, 496, 19

Lira P. et al., 2018, ApJ, 865, 56

Lu K.-X. et al., 2016, ApJ, 827, 118

Malik U. et al., 2022, MNRAS, 516, 3238

Malik U. et al., 2023, MNRAS, 520, 2009

Martínez-Aldama M. L., Czerny B., Kawka D., Karas V., Panda S., Zajaček M., Życki P. T., 2019, ApJ, 883, 170

Metzroth K. G., Onken C. A., Peterson B. M., 2006, ApJ, 647, 901

Morganson E. et al., 2018, PASP, 130, 074501

Pei L. et al., 2014, ApJ, 795, 38

Penton A. et al., 2022, MNRAS, 509, 4008

Peterson B. M., 1993, PASP, 105, 247

Peterson B. M., Horne K., 2004, Astron. Nachr., 325, 248

Peterson B. M., Wanders I., Horne K., Collier S., Alexander T., Kaspi S., Maoz D., 1998, PASP, 110, 660

Peterson B. M. et al., 2005, ApJ, 632, 799

Rakshit S. et al., 2019, ApJ, 886, 93

Sharp R. et al., 2006, in McLean I. S., Iye M., eds, SPIE Conf. Ser. Vol. 6269, 62690G, preprint (astro-ph/0606137)

Shen Y. et al., 2011, ApJS, 194, 45

Shen Y. et al., 2015, ApJS, 216, 4

Shen Y. et al., 2019, ApJ, 883, L14

Sun M., Grier C. J., Peterson B. M., 2018, PyCCF: Python Cross Correlation Function for reverberation mapping studies., record (ascl:1805.032)

Swann E. et al., 2019, The Messenger, 175, 58

Tie S. S. et al., 2017, AJ, 153, 107

Trakhtenbrot B., Netzer H., 2012, MNRAS, 427, 3081

Trevese D., Perna M., Vagnetti F., Saturni F. G., Dadina M., 2014, ApJ, 795, 164

U V. et al., 2022, ApJ, 925, 52

Vanden Berk D. E. et al., 2001, AJ, 122, 549

Virtanen P. et al., 2020, Nature Methods, 17, 261

Wang J.-M. et al., 2014, ApJ, 793, 108

Watson D., Denney K. D., Vestergaard M., Davis T. M., 2011, ApJ, 740, L49

Woo J.-H., Yoon Y., Park S., Park D., Kim S. C., 2015, ApJ, 801, 38

Yu Z. et al., 2021, MNRAS, 507, 3771

Yu Z. et al., 2023, MNRAS, 522, 4132

Yuan F. et al., 2015, MNRAS, 452, 3047

Zajaček M. et al., 2020, ApJ, 896, 146

Zajaček M. et al., 2021, ApJ, 912, 10

Zhang Z.-X. et al., 2019, ApJ, 876, 49

APPENDIX A: SOURCE PROPERTIES

The source properties are given for the Hβ sample of 69 AGN in Table A1, the Mg II sample of 450 AGN in Table A2, and the C IV sample of 290 AGN in Table A3.

Table A1. Properties for our OzDES Hβ stacking sample. Columns left to right: DES name (J2000), redshift, r-band apparent AB magnitude, monochromatic luminosity at 5100 Å. The superscript a flags sources that also have Mg II data.

DES ID	z	m_r	$\log(\lambda L_{5100})$ (erg s^{-1})
DES J002802.42−424913.52	0.127	17.88	43.67
DES J033633.16−284027.18	0.129	17.73	43.74
DES J022024.92−061731.51	0.139	18.04	43.69
DES J003515.60−433357.64	0.145	17.75	43.84
DES J003245.59−421441.67	0.183	18.85	43.62
DES J025007.02+002525.49	0.198	18.02	44.03
DES J024347.34−005354.84	0.237	19.19	43.73
DES J024340.97−002601.16	0.268	19.16	43.86
DES J025021.72−005413.02	0.271	19.87	43.59
DES J025211.61−003629.35	0.294	20.10	43.58
DES J034028.46−292902.41	0.310	18.09	44.43
DES J022249.67−051453.01	0.314	19.03	44.07
DES J025240.59−002117.04	0.315	20.37	43.53
DES J022851.50−051223.00	0.317	18.01	44.48
DES J003954.13−440509.97	0.332	19.53	43.92
DES J022330.16−054758.06	0.354	19.87	43.85
DES J024325.53−000412.67	0.356	20.47	43.62
DES J024902.03−004322.43	0.360	20.75	43.52
DES J024320.36−001825.41	0.373	19.47	44.07
DES J024519.82−010245.63	0.381	20.46	43.69
DES J024225.86−004142.50	0.383	20.74	43.59
DES J003622.82−424759.11	0.390	21.02	43.49
DES J004009.06−431255.29	0.434	19.04	44.40
DES J003834.47−433807.12	0.453	20.61	43.82
DES J025042.90−004138.74	0.457	20.54	43.86
DES J022258.90−045852.28	0.466	19.77	44.20
DES J024712.89−011106.21	0.486	20.56	43.92
DES J024211.93−010959.69	0.488	20.18	44.08
DES J024538.29−004705.32	0.488	20.49	43.96
DES J003017.47−422446.39	0.491	18.48	44.77
DES J022133.82−054842.69	0.501	18.77	44.67
DES J024643.04−013149.55	0.502	19.32	44.45
DES J033002.93−273248.31	0.527	20.33	44.10
DES J003552.21−423352.14	0.530	21.29	43.72
DES J022019.61−060729.77	0.541	20.07	44.23
DES J021910.57−055114.76	0.558	19.49	44.49
DES J025119.79−004831.62	0.559	19.98	44.30
DES J033758.00−294618.46	0.561	19.27	44.58
DES J024939.57+000700.39	0.564	20.90	43.94
DES J024646.73−001220.60	0.564	19.73	44.41
DES J022717.88−051623.78	0.566	20.87	43.95
DES J033946.12−295030.94	0.582	20.33	44.20
DES J003114.43−424227.81	0.591	20.53	44.13
DES J033905.07−292134.36	0.600	18.66	44.89
DES J022329.27−045451.85	0.604	20.78	44.05
DES J033738.50−272306.75	0.613	18.60	44.94
DES J022246.23−041450.67	0.614	19.94	44.40
DES J024651.86−010732.56	0.622	20.36	44.25
DES J033910.13−264311.77	0.622	21.39	43.84
DES J024442.77−004223.14	0.628	19.92	44.43
DES J021923.29−045148.69	0.630	19.36	44.66
DES J033051.45−271254.90	0.633	20.24	44.31
DES J032718.70−281857.85	0.634	19.52	44.60
DES J002904.43−425243.04	0.644	19.54	44.61
DES J021820.49−050426.42	0.650	19.59	44.60

Table A1 – *continued*

DES ID	z	m_r	$\log(\lambda L_{5100})$ (erg s^{-1})
DES J034056.37−293339.67	0.652	20.44	44.26
DES J003013.70−425733.44 [a]	0.654	20.31	44.32
DES J024533.65−000744.91 [a]	0.655	19.66	44.58
DES J003010.25−423356.22 [a]	0.667	20.14	44.40
DES J003231.39−433511.71 [a]	0.679	20.39	44.32
DES J004334.89−440546.53 [a]	0.681	19.62	44.63
DES J021952.14−040919.86 [a]	0.692	20.30	44.37
DES J022452.19−040519.38 [a]	0.695	19.85	44.55
DES J002906.71−423904.49 [a]	0.703	18.69	45.03
DES J021514.27−053321.33 [a]	0.703	20.01	44.50
DES J033819.34−274346.33 [a]	0.706	18.81	44.98
DES J022617.85−043108.99 [a]	0.708	19.52	44.70
DES J021524.99−045353.83 [a]	0.714	20.51	44.31
DES J021808.24−045845.20 [a]	0.716	18.18	45.25

Table A2. Properties for our OzDES Mg II stacking sample. Columns left to right: DES name (J2000), redshift, *r*-band apparent AB magnitude, monochromatic luminosity at 3000 Å. The superscript *a* flags sources that also have Hβ data, and *b* flags sources that also have C IV data.

DES ID	z	m_r	$\log(\lambda L_{3000})$ (erg s^{-1})
DES J003013.70−425733.44 [a]	0.654	20.31	44.47
DES J024533.65−000744.91 [a]	0.655	19.66	44.73
DES J003010.25−423356.22 [a]	0.667	20.14	44.56
DES J003231.39−433511.71 [a]	0.679	20.39	44.47
DES J004334.89−440546.53 [a]	0.681	19.62	44.78
DES J021952.14−040919.86 [a]	0.692	20.30	44.53
DES J022452.19−040519.38 [a]	0.695	19.85	44.71
DES J002906.71−423904.49 [a]	0.703	18.69	45.18
DES J021514.27−053321.33 [a]	0.703	20.01	44.66
DES J033819.34−274346.33 [a]	0.706	18.81	45.14
DES J022617.85−043108.99 [a]	0.708	19.52	44.86
DES J021524.99−045353.83 [a]	0.714	20.51	44.47
DES J021808.24−045845.20 [a]	0.716	18.18	45.40
DES J033545.58−293216.49	0.724	20.30	44.56
DES J024126.71−004526.12	0.727	18.92	45.12
DES J033227.00−274105.28	0.730	19.81	44.77
DES J024727.97−013008.97	0.741	20.26	44.60
DES J022421.67−064613.71	0.755	20.48	44.53
DES J032724.94−274202.77	0.756	19.78	44.81
DES J021902.96−062107.22	0.758	20.42	44.55
DES J022244.40−043346.88	0.761	19.23	45.03
DES J025048.65+000207.62	0.766	19.12	45.08
DES J003155.93−434225.34	0.768	19.30	45.01
DES J021705.51−042253.46	0.788	20.24	44.66
DES J033459.10−293317.41	0.801	19.99	44.77
DES J032850.20−271207.84	0.802	19.42	45.00
DES J003350.95−435606.17	0.806	19.61	44.93
DES J022155.25−064916.59	0.807	18.06	45.55
DES J024801.09−004015.63	0.811	20.05	44.76
DES J025146.78−004035.49	0.813	19.63	44.93
DES J022326.46−045705.99	0.825	20.72	44.50
DES J025100.99+004802.99	0.829	20.03	44.78
DES J021628.43−040147.11	0.831	19.52	44.99
DES J033246.02−282232.12	0.839	20.07	44.78
DES J033328.93−275641.20	0.839	20.29	44.69
DES J022255.89−051351.61	0.849	19.01	45.21
DES J004042.70−440341.05	0.851	19.78	44.91
DES J033332.81−282220.34	0.858	19.14	45.17
DES J024637.94−004105.24	0.859	20.10	44.79
DES J033137.70−284808.03	0.862	21.68	44.16
DES J033230.63−284750.36	0.862	20.70	44.55
DES J033235.64−290202.05	0.866	19.33	45.10

Table A2 – *continued*

DES ID	z	m_r	$\log(\lambda L_{3000})$ (erg s^{-1})
DES J003527.80−443411.36	0.869	19.90	44.88
DES J002831.10−421538.06	0.871	18.98	45.25
DES J033523.52−280723.67	0.871	17.25	45.94
DES J003331.34−441039.28	0.878	19.64	44.99
DES J004020.36−432053.98	0.880	19.49	45.05
DES J002641.26−424900.31	0.882	19.95	44.87
DES J021557.63−045009.52	0.884	18.73	45.36
DES J003301.72−440750.87	0.886	19.86	44.91
DES J024831.08−005025.58	0.887	20.42	44.69
DES J002951.05−433629.34	0.892	20.66	44.60
DES J002702.17−431755.99	0.900	20.15	44.81
DES J021413.01−042930.02	0.901	19.08	45.24
DES J024159.74−010512.38	0.904	20.16	44.81
DES J024357.90−011330.42	0.905	20.22	44.79
DES J022440.72−043657.71	0.907	20.14	44.82
DES J025217.48−005249.30	0.912	20.52	44.67
DES J002930.76−432724.34	0.914	18.35	45.54
DES J003437.73−424318.36	0.915	19.09	45.25
DES J033520.08−284258.52	0.931	20.14	44.84
DES J003435.26−441127.90	0.933	19.40	45.14
DES J024425.38−004652.99	0.937	18.90	45.34
DES J003809.48−435241.29	0.937	19.40	45.14
DES J033435.50−282812.24	0.940	19.88	44.95
DES J002926.51−431250.54	0.944	18.96	45.33
DES J002917.61−433759.92	0.951	18.58	45.48
DES J024237.79−012354.10	0.957	19.65	45.06
DES J033435.49−283631.56	0.963	20.09	44.89
DES J022049.53−053731.08	0.974	20.00	44.94
DES J022344.57−064039.01	0.983	20.83	44.61
DES J022712.98−044636.25	0.983	18.13	45.69
DES J033945.79−275333.88	0.984	21.29	44.43
DES J033404.10−275629.92	0.984	20.75	44.65
DES J033339.36−281724.26	0.987	20.02	44.94
DES J033509.98−283255.27	0.993	18.03	45.74
DES J002933.85−435240.66	0.995	18.06	45.73
DES J022114.78−050832.95	0.996	20.60	44.72
DES J032853.99−281706.94	1.000	20.29	44.84
DES J024514.00−003535.43	1.005	19.41	45.20
DES J025237.80−004627.79	1.008	19.49	45.17
DES J021500.22−043007.46	1.012	19.76	45.06
DES J024300.44−003030.10	1.018	20.52	44.76
DES J022449.86−043025.80	1.024	20.44	44.80
DES J024924.67+002536.38	1.025	19.93	45.00
DES J033531.95−271825.19	1.029	19.14	45.32
DES J033408.25−274337.81	1.029	20.69	44.70
DES J003914.17−443844.22	1.033	19.62	45.13
DES J033854.56−291001.97	1.049	20.21	44.91
DES J032831.40−285249.79	1.050	20.47	44.80
DES J022104.63−044239.89	1.052	20.25	44.89
DES J002826.18−433829.09	1.063	20.90	44.64
DES J003710.86−444048.06	1.067	18.53	45.59
DES J033810.75−275153.11	1.077	19.45	45.23
DES J033948.28−275438.98	1.077	17.51	46.01
DES J021817.44−045112.40	1.083	19.25	45.32
DES J002949.39−434806.73	1.088	19.29	45.31
DES J025228.55+003109.14	1.110	18.81	45.52
DES J025128.38+001144.60	1.117	20.17	44.98
DES J033045.54−284150.29	1.119	19.57	45.22
DES J003145.76−421747.61	1.129	19.38	45.30
DES J003834.04−432457.69	1.133	20.29	44.94
DES J034020.28−291750.48	1.135	18.28	45.75
DES J003536.95−443104.40	1.136	20.06	45.04
DES J002639.87−432307.71	1.139	19.58	45.23
DES J024617.07−000602.60	1.143	18.42	45.70

Table A2 – *continued*

DES ID	z	m_r	$\log(\lambda L_{3000})$ (erg s^{-1})
DES J003452.22−434613.99	1.146	20.77	44.76
DES J024854.80+001054.04	1.146	19.57	45.24
DES J033836.19−295113.53	1.148	20.95	44.69
DES J003444.53−433749.06	1.153	20.12	45.03
DES J021631.35−043207.93	1.155	19.74	45.18
DES J022501.68−040754.18	1.157	19.67	45.21
DES J003332.28−430526.16	1.159	18.53	45.67
DES J022718.54−053124.86	1.159	21.06	44.66
DES J033350.23−284244.42	1.161	21.12	44.63
DES J021849.86−035835.29	1.162	19.18	45.41
DES J033612.01−290152.96	1.164	19.58	45.25
DES J033353.02−283022.38	1.165	18.51	45.68
DES J033429.54−293904.49	1.167	20.57	44.86
DES J033416.89−274504.73	1.168	20.12	45.04
DES J033719.99−262418.84	1.169	19.56	45.27
DES J003725.23−431710.85	1.173	19.94	45.12
DES J022556.83−045853.05	1.180	21.09	44.66
DES J022823.19−041223.67	1.181	17.57	46.07
DES J022533.79−050801.95	1.183	18.40	45.74
DES J033744.23−262559.74	1.187	18.85	45.56
DES J025036.99−002408.04	1.195	20.68	44.84
DES J033335.92−264915.24	1.199	19.99	45.12
DES J024840.98−001228.80	1.199	19.11	45.47
DES J003848.77−434518.55	1.200	21.03	44.70
DES J003549.87−424526.29	1.208	20.26	45.02
DES J033627.43−294149.95	1.218	18.59	45.69
DES J022212.40−061246.20	1.220	20.71	44.85
DES J022108.60−061753.21	1.225	20.00	45.13
DES J033534.69−283149.26	1.225	19.71	45.25
DES J022134.35−062941.64	1.228	20.71	44.85
DES J024544.78−004415.24	1.229	19.82	45.21
DES J022423.52−065001.40	1.229	20.15	45.08
DES J022023.48−064959.19	1.232	20.35	45.00
DES J033525.23−270200.72	1.233	19.31	45.42
DES J022055.16−060136.43	1.234	20.55	44.92
DES J003703.65−434759.50	1.236	19.87	45.20
DES J004111.46−441014.38	1.237	20.20	45.06
DES J033211.42−284323.98	1.237	21.86	44.40
DES J033928.30−291714.73	1.241	20.08	45.12
DES J003125.94−434743.50	1.243	20.25	45.05
DES J024918.24−001731.03	1.244	19.82	45.22
DES J021906.15−063000.89	1.250	20.12	45.10
DES J002743.35−425258.79	1.252	19.94	45.18
DES J033635.40−273427.02	1.254	20.17	45.09
DES J003322.53−442412.38	1.257	19.47	45.37
DES J022445.39−065556.80	1.261	21.11	44.72
DES J022115.87−062217.45	1.273	18.82	45.64
DES J024306.66−002531.29	1.279	20.36	45.03
DES J022245.85−041932.10	1.283	20.61	44.93
DES J034106.19−291410.86	1.287	21.20	44.70
DES J022529.40−050946.39	1.288	20.93	44.81
DES J024939.57−001157.73	1.295	20.97	44.80
DES J024621.09−000152.02	1.296	18.64	45.73
DES J021957.86−060534.66	1.296	20.74	44.89
DES J025323.64+000446.97	1.297	20.18	45.12
DES J022024.34−061401.95	1.297	21.31	44.66
DES J033911.64−290601.76	1.298	20.06	45.16
DES J025224.97+001308.30	1.300	20.68	44.92
DES J003819.73−443134.02	1.305	18.80	45.67
DES J024455.17−002501.41	1.308	19.29	45.48
DES J034032.74−270521.33	1.310	20.91	44.83
DES J024811.51−012609.51	1.313	19.29	45.48
DES J003639.49−430400.30	1.317	20.20	45.12
DES J033308.48−285832.12	1.318	19.72	45.31
DES J025005.69−004054.86	1.320	20.41	45.04

Table A2 – *continued*

DES ID	z	m_r	$\log(\lambda L_{3000})$ (erg s^{-1})
DES J033030.59−282135.43	1.322	18.89	45.65
DES J022024.93−053744.40	1.322	21.14	44.75
DES J003245.16−440451.51	1.323	20.84	44.87
DES J033216.20−273930.61	1.324	20.60	44.96
DES J033525.44−265531.09	1.325	17.55	46.19
DES J033939.33−272454.08	1.325	19.19	45.53
DES J033303.99−271531.43	1.329	20.13	45.16
DES J033533.91−264847.02	1.330	20.25	45.11
DES J002855.47−434210.06	1.331	20.14	45.15
DES J024214.97−003131.71	1.332	19.93	45.24
DES J033057.32−284737.42	1.335	20.99	44.81
DES J033635.49−263735.76	1.336	19.99	45.22
DES J033824.55−263527.10	1.340	19.65	45.35
DES J024652.16−011242.95	1.340	19.44	45.44
DES J024326.61−002056.06	1.345	20.51	45.01
DES J022351.09−053750.25	1.347	18.61	45.77
DES J033723.98−294917.22	1.351	19.00	45.62
DES J022446.16−050827.57	1.357	18.85	45.69
DES J022436.17−065912.26	1.360	20.78	44.91
DES J022419.74−062142.31	1.361	18.52	45.82
DES J025324.69−002655.67	1.364	19.41	45.47
DES J003922.97−430230.45	1.369	19.71	45.35
DES J024234.93−010351.83	1.371	19.46	45.45
DES J025252.02−002211.61	1.371	20.68	44.96
DES J025318.92+001559.61	1.374	20.92	44.87
DES J002857.80−424644.03	1.377	18.74	45.74
DES J033923.53−265229.48	1.379	20.57	45.01
DES J034027.16−285641.30	1.379	18.74	45.74
DES J004055.63−441249.41	1.383	20.42	45.08
DES J033444.13−264215.40	1.384	19.57	45.42
DES J003738.22−443838.25	1.385	20.13	45.19
DES J025145.09−004639.64	1.386	19.81	45.32
DES J021749.09−041215.57	1.386	20.13	45.19
DES J022815.08−041942.59	1.387	20.10	45.21
DES J024746.99−011334.42	1.389	20.63	44.99
DES J003814.08−433314.92	1.390	18.27	45.94
DES J022032.25−044217.60	1.401	20.25	45.16
DES J021451.07−044236.60	1.401	20.97	44.87
DES J022446.95−055739.13	1.409	20.88	44.91
DES J022402.07−062943.14	1.412	20.17	45.20
DES J022124.53−050205.23	1.415	19.02	45.66
DES J032942.54−272012.09	1.415	19.94	45.29
DES J003827.69−433518.19	1.419	19.96	45.28
DES J022436.64−063255.90	1.423	20.95	44.89
DES J024935.55−001336.76	1.423	19.99	45.28
DES J024606.20−005531.75	1.426	20.38	45.12
DES J003052.76−430301.10	1.428	19.39	45.52
DES J024929.19−002104.15	1.428	19.00	45.67
DES J022216.72−041719.73	1.432	19.89	45.32
DES J033918.13−293008.14	1.436	21.12	44.83
DES J024340.09−001749.37	1.436	19.68	45.41
DES J024753.20−002137.75	1.437	20.16	45.22
DES J024212.65−010339.46	1.438	20.77	44.97
DES J033435.10−262635.67	1.441	19.45	45.50
DES J021939.92−061407.00	1.446	20.60	45.05
DES J022041.19−055039.80	1.454	20.27	45.19
DES J022006.60−061936.36	1.460	19.83	45.37
DES J033630.87−291753.39	1.462	19.63	45.45
DES J024820.90−002546.67	1.463	19.98	45.31
DES J025030.77−000801.72	1.466	18.31	45.98
DES J002940.83−424308.05	1.472	19.66	45.44
DES J025024.52−001419.03	1.472	19.98	45.31
DES J033310.16−282433.18	1.476	20.99	44.91
DES J003253.01−435626.33	1.476	20.01	45.30
DES J022644.23−040720.13	1.479	19.76	45.41

Table A2 – *continued*

DES ID	z	m_r	$\log(\lambda L_{3000})$ (erg s^{-1})
DES J003035.42−433249.60	1.480	18.77	45.80
DES J024944.09+003317.50	1.480	19.71	45.43
DES J003053.45−432344.99	1.490	20.58	45.09
DES J033213.36−283621.03	1.492	20.36	45.18
DES J003232.61−433303.00	1.492	19.77	45.41
DES J032604.02−275629.36	1.494	18.53	45.91
DES J022429.11−045807.69	1.498	20.30	45.20
DES J003621.41−435139.13	1.501	20.21	45.24
DES J034101.59−293056.44	1.504	20.49	45.13
DES J022350.77−043158.10	1.504	19.90	45.37
DES J021620.91−053417.45	1.508	20.11	45.29
DES J033253.86−283139.33	1.509	20.61	45.09
DES J024959.77−000104.11	1.512	20.09	45.30
DES J024920.97+004206.39	1.524	20.66	45.08
DES J021630.87−042051.45	1.528	19.90	45.39
DES J024455.45−011500.42	1.529	20.51	45.15
DES J033951.49−291713.89	1.530	20.83	45.02
DES J032643.99−280657.07	1.532	19.73	45.46
DES J004232.48−440757.18	1.532	18.38	46.00
DES J003207.44−433049.00	1.533	19.65	45.50
DES J033400.71−271540.89	1.538	20.04	45.35
DES J025254.85−420236.96	1.541	20.28	45.25
DES J022338.53−063246.90	1.546	21.24	44.88
DES J025311.70−004241.62	1.547	20.36	45.23
DES J022059.48−044917.03	1.547	18.51	45.97
DES J033355.67−282651.58	1.551	20.39	45.22
DES J033853.03−271735.34	1.553	21.16	44.91
DES J022509.54−040838.19	1.553	20.43	45.21
DES J003006.53−435107.85	1.555	20.46	45.20
DES J022520.75−041246.56	1.559	20.38	45.23
DES J022154.21−061941.56	1.559	20.13	45.33
DES J021612.83−044634.12	1.560	19.86	45.44
DES J003433.01−423342.34	1.561	20.28	45.27
DES J033410.83−280949.16	1.562	21.54	44.77
DES J033058.53−275148.31	1.562	20.90	45.03
DES J025318.76+000414.19	1.563	20.15	45.33
DES J033101.15−275125.44	1.563	19.12	45.74
DES J004016.88−442556.16	1.565	20.24	45.29
DES J003829.91−434454.27	1.567	17.83	46.26
DES J003858.70−443045.51	1.569	19.95	45.41
DES J003653.08−435441.53	1.572	19.32	45.67
DES J033211.64−273726.16	1.574	19.22	45.71
DES J033325.92−290142.07	1.574	20.77	45.09
DES J022422.63−061943.20	1.575	21.53	44.78
DES J002939.03−431253.68	1.577	20.70	45.12
DES J033553.51−275044.68	1.578	18.99	45.80
DES J025148.53−004637.61	1.579	19.50	45.60
DES J003413.73−432600.36	1.588	21.23	44.91
DES J022733.98−042523.34	1.590	20.57	45.18
DES J032801.84−273815.71	1.590	20.14	45.35
DES J003952.64−442753.23	1.591	20.03	45.40
DES J003254.79−423926.69	1.597	19.28	45.70
DES J003307.13−424912.19	1.598	20.49	45.22
DES J024603.67−003211.73 [b]	1.601	18.99	45.82
DES J033304.62−291230.05 [b]	1.603	20.19	45.34
DES J024823.76−010002.36	1.603	20.48	45.23
DES J022152.62−062834.38 [b]	1.604	20.96	45.03
DES J033617.72−300224.76 [b]	1.605	19.88	45.47
DES J033604.07−292659.88 [b]	1.610	20.07	45.39
DES J021505.09−045855.98	1.610	19.33	45.69
DES J033721.40−292323.42 [b]	1.612	19.99	45.43
DES J033918.18−293142.92 [b]	1.612	21.04	45.01
DES J033407.62−291607.55 [b]	1.615	19.59	45.59
DES J002950.78−423801.20 [b]	1.616	20.69	45.15

Table A2 – *continued*

DES ID	z	m_r	$\log(\lambda L_{3000})$ (erg s^{-1})
DES J003723.59−442258.09 [b]	1.618	19.98	45.44
DES J033139.43−284939.85	1.619	20.93	45.06
DES J003426.66−422807.96	1.622	21.07	45.00
DES J022016.53−043209.15	1.624	21.22	44.94
DES J025225.52+003405.92	1.624	19.97	45.44
DES J021600.36−043829.30 [b]	1.624	20.33	45.30
DES J033220.31−280214.82	1.625	21.11	44.99
DES J021947.13−043754.70 [b]	1.626	20.63	45.18
DES J033835.80−274224.52 [b]	1.629	20.00	45.44
DES J003501.58−425344.26 [b]	1.632	19.98	45.45
DES J003454.09−425716.21 [b]	1.633	20.62	45.19
DES J022247.88−043330.04 [b]	1.635	20.24	45.34
DES J003234.33−431937.83 [b]	1.641	19.40	45.68
DES J022224.82−062626.69 [b]	1.641	20.16	45.38
DES J025254.18−001119.67 [b]	1.641	21.25	44.94
DES J022716.52−050008.33 [b]	1.642	20.50	45.24
DES J022337.73−062354.60	1.646	20.91	45.08
DES J034044.75−270720.15	1.647	21.14	44.99
DES J024207.50−004423.41	1.647	22.32	44.52
DES J033437.58−275826.84 [b]	1.648	18.69	45.97
DES J022008.73−045905.31 [b]	1.649	20.52	45.24
DES J033657.91−274244.39 [b]	1.649	20.14	45.39
DES J003015.00−430333.45 [b]	1.650	19.97	45.46
DES J022029.60−051022.59 [b]	1.652	20.68	45.18
DES J024422.20−011247.11	1.654	20.14	45.40
DES J022228.25−060547.60	1.658	20.34	45.32
DES J022319.01−070927.36	1.659	21.32	44.93
DES J003143.64−425420.21 [b]	1.662	20.03	45.44
DES J022208.15−065550.48	1.662	21.12	45.01
DES J003245.74−431453.18	1.671	20.78	45.15
DES J003548.43−431444.38 [b]	1.673	20.47	45.27
DES J022424.16−043229.83 [b]	1.674	20.32	45.34
DES J025340.94+001110.20 [b]	1.675	18.31	46.14
DES J024906.74+000823.79	1.677	20.68	45.19
DES J003956.32−442047.73 [b]	1.680	20.08	45.44
DES J021439.12−051355.34	1.683	20.96	45.08
DES J033903.66−293326.48 [b]	1.684	21.85	44.73
DES J003948.24−445323.16 [b]	1.684	19.59	45.63
DES J025429.12−000404.45	1.685	21.98	44.68
DES J003635.93−434636.05 [b]	1.689	19.90	45.51
DES J025220.53+002735.19 [b]	1.690	19.86	45.53
DES J033341.61−284603.55	1.693	21.02	45.07
DES J021902.58−044628.33 [b]	1.694	19.92	45.51
DES J025356.07+001057.54 [b]	1.695	19.47	45.69
DES J003325.69−434826.13 [b]	1.696	20.26	45.37
DES J024527.72−010602.84 [b]	1.696	20.05	45.46
DES J003030.66−420243.68	1.696	20.65	45.22
DES J033457.77−274956.61	1.700	21.58	44.85
DES J022445.77−061149.99 [b]	1.701	20.19	45.40
DES J003213.12−434553.39	1.706	17.34	46.55
DES J003256.53−441451.15	1.708	19.89	45.53
DES J022907.98−045102.02	1.714	20.91	45.12
DES J022014.98−062253.15 [b]	1.716	19.91	45.52
DES J024207.18−002818.79	1.716	19.83	45.56
DES J003721.82−443051.40	1.716	20.33	45.36
DES J003221.43−423908.40	1.719	21.21	45.01
DES J024632.55−003439.14 [b]	1.724	19.87	45.55
DES J022134.97−070831.84 [b]	1.728	20.70	45.22
DES J032940.47−275143.61 [b]	1.730	19.87	45.55
DES J022602.20−061626.10 [b]	1.736	19.97	45.51
DES J003734.68−441539.48	1.738	20.15	45.44
DES J024611.20−003134.33	1.738	20.52	45.29
DES J021647.25−044029.81	1.746	21.58	44.87
DES J003206.50−425325.23 [b]	1.750	19.84	45.57

Table A2 – *continued*

DES ID	z	m_r	$\log(\lambda L_{3000})$ (erg s^{-1})
DES J033814.33−294213.78 [b]	1.750	19.94	45.53
DES J002920.73−420425.08	1.750	19.66	45.64
DES J033453.60−264121.34 [b]	1.751	20.14	45.45
DES J033817.74−290324.90 [b]	1.753	19.61	45.67
DES J021732.31−052950.95	1.755	21.84	44.77
DES J033211.80−284257.07	1.755	20.26	45.41
DES J022115.04−043155.51 [b]	1.757	21.33	44.98
DES J033452.89−265215.54 [b]	1.757	19.10	45.87
DES J033451.51−280041.23	1.758	21.49	44.92
DES J022117.44−063856.45 [b]	1.763	19.83	45.58
DES J024140.99−012712.41	1.768	20.33	45.39
DES J024257.19−004549.41 [b]	1.770	21.08	45.09
DES J022119.91−045948.62 [b]	1.770	20.76	45.22
DES J003120.86−425145.98 [b]	1.771	20.14	45.47
DES J002859.58−423239.47	1.776	19.43	45.75
DES J022024.08−045709.48	1.776	19.84	45.59
DES J033912.33−293043.57	1.778	21.35	44.98
DES J004029.04−441704.97 [b]	1.783	20.04	45.51
DES J003255.12−435757.56 [b]	1.784	20.07	45.50
DES J022533.36−065917.56	1.784	18.95	45.95
DES J032759.97−271921.90 [b]	1.785	20.37	45.38
DES J024222.95−011527.57 [b]	1.785	20.24	45.43
DES J032914.81−290130.69	1.787	20.50	45.33
DES J033328.60−290314.66 [b]	1.787	19.58	45.70
DES J022027.32−045115.53 [b]	1.788	21.14	45.08
DES J033922.52−292857.78	1.789	21.27	45.02
DES J022002.08−050101.91 [b]	1.791	19.69	45.66
DES J022751.50−044252.66 [b]	1.795	20.60	45.30
DES J003939.41−444612.90 [b]	1.797	20.17	45.47
DES J022503.11−065258.79 [b]	1.798	20.09	45.50
DES J032835.62−274406.09 [b]	1.800	19.94	45.56
DES J033722.89−274020.85 [b]	1.804	19.93	45.57
DES J003921.57−441844.65	1.813	19.91	45.58
DES J003920.50−440441.16 [b]	1.814	19.79	45.63
DES J003739.59−432521.40 [b]	1.815	20.40	45.39
DES J022231.63−043256.29	1.816	19.67	45.68
DES J033047.84−281521.39	1.818	21.53	44.94
DES J034001.87−270136.24	1.819	21.05	45.13
DES J004156.96−435856.50	1.821	20.36	45.41
DES J024635.61−000850.46 [b]	1.822	19.26	45.85
DES J033002.51−274858.28 [b]	1.823	20.70	45.27
DES J033017.79−280231.25	1.823	20.61	45.31
DES J033548.18−290943.65 [b]	1.826	20.33	45.42
DES J022352.09−064029.96 [b]	1.827	20.50	45.35
DES J022409.89−044718.00 [b]	1.832	20.11	45.51
DES J033319.58−290431.65 [b]	1.833	20.73	45.27
DES J024716.32−010401.36 [b]	1.834	21.10	45.12
DES J021958.13−041707.68	1.837	21.09	45.12
DES J033222.47−285935.09 [b]	1.837	20.68	45.29
DES J033301.69−275818.80 [b]	1.840	20.94	45.19
DES J004014.18−431716.29 [b]	1.842	19.87	45.62
DES J021643.70−052236.21	1.844	20.57	45.34
DES J021903.49−043935.00 [b]	1.845	20.48	45.37
DES J033539.94−265025.37	1.846	19.68	45.69
DES J024737.50−000458.97 [b]	1.847	19.88	45.62
DES J024608.67−013933.97 [b]	1.848	19.68	45.70
DES J022515.35−044008.91 [b]	1.850	19.82	45.64
DES J025038.68−004739.06 [b]	1.856	18.67	46.10
DES J002729.28−431501.02 [b]	1.863	19.67	45.71
DES J024723.54−002536.48 [b]	1.864	19.42	45.81
DES J022845.57−043350.18 [b]	1.864	17.41	46.61
DES J024748.87−000147.41 [b]	1.868	19.58	45.75
DES J024133.65−010724.20 [b]	1.874	20.86	45.24
DES J003940.80−443718.32 [b]	1.875	19.49	45.79

Table A2 – *continued*

DES ID	z	m_r	$\log(\lambda L_{3000})$ (erg s^{-1})
DES J024838.93−000325.87	1.876	20.61	45.34
DES J022047.63−051835.83 [b]	1.878	19.55	45.77ff
DES J021544.02−053607.56	1.885	21.31	45.06
DES J025513.03+000639.59	1.885	19.78	45.68
DES J021707.96−055152.07 [b]	1.885	19.70	45.71
DES J033145.20−275435.75 [b]	1.891	21.19	45.12
DES J033225.90−282208.45	1.894	21.55	44.97
DES J022213.31−041030.05	1.903	20.14	45.54
DES J024242.50−002212.87 [b]	1.904	20.57	45.37
DES J022828.19−040044.25 [b]	1.905	18.31	46.28
DES J003626.44−430820.66 [b]	1.907	19.80	45.68
DES J022050.39−061748.80 [b]	1.908	21.89	44.85
DES J021953.45−061123.39 [b]	1.910	19.90	45.64
DES J003150.13−432726.88 [b]	1.912	18.68	46.13
DES J022328.88−040134.71 [b]	1.915	19.82	45.68
DES J033739.88−272045.97 [b]	1.916	19.21	45.92
DES J033924.44−271250.15 [b]	1.918	20.52	45.40
DES J025428.31+002418.43 [b]	1.918	20.42	45.44
DES J033415.37−265535.62 [b]	1.922	19.85	45.67
DES J033011.77−283636.65 [b]	1.922	20.99	45.21
DES J022327.85−040119.16 [b]	1.922	20.81	45.29
DES J024639.22−012731.85 [b]	1.923	20.34	45.47

Table A3. Properties for our OzDES C IV stacking sample. Columns left to right: DES name (J2000), redshift, r-band apparent AB magnitude, monochromatic luminosity at 1350 Å. The superscript *b* flags sources that also have Mg II data.

DES ID	z	m_r	$\log(\lambda L_{1350})$ (erg s^{-1})
DES J024603.67−003211.73 [a]	1.601	18.99	45.93
DES J033304.62−291230.05 [a]	1.603	20.19	45.45
DES J022152.62−062834.38 [a]	1.604	20.96	45.14
DES J033617.72−300224.76 [a]	1.605	19.88	45.57
DES J033604.07−292659.88 [a]	1.610	20.07	45.50
DES J033721.40−292323.42 [a]	1.612	19.99	45.53
DES J033918.18−293142.92 [a]	1.612	21.04	45.11
DES J033407.62−291607.55 [a]	1.615	19.59	45.70
DES J002950.78−423801.20 [a]	1.616	20.69	45.26
DES J003723.59−442258.09 [a]	1.618	19.98	45.54
DES J021600.36−043829.30 [a]	1.624	20.33	45.41
DES J021947.13−043754.70 [a]	1.626	20.63	45.29
DES J033835.80−274224.52 [a]	1.629	20.00	45.54
DES J003501.58−425344.26 [a]	1.632	19.98	45.55
DES J003454.09−425716.21 [a]	1.633	20.62	45.30
DES J022247.88−043330.04 [a]	1.635	20.24	45.45
DES J003234.33−431937.83 [a]	1.641	19.40	45.79
DES J022224.82−062626.69 [a]	1.641	20.16	45.48
DES J025254.18−001119.67 [a]	1.641	21.25	45.05
DES J022716.52−050008.33 [a]	1.642	20.50	45.35
DES J033437.58−275826.84 [a]	1.648	18.69	46.08
DES J022008.73−045905.31 [a]	1.649	20.52	45.35
DES J033657.91−274244.39 [a]	1.649	20.14	45.50
DES J003015.00−430333.45 [a]	1.650	19.97	45.57
DES J022029.60−051022.59 [a]	1.652	20.68	45.28
DES J003143.64−425420.21 [a]	1.662	20.03	45.55
DES J003548.43−431444.38 [a]	1.673	20.47	45.38
DES J022424.16−043229.83 [a]	1.674	20.32	45.44
DES J025340.94+001110.20 [a]	1.675	18.31	46.25
DES J003956.32−442047.73 [a]	1.680	20.08	45.54
DES J033903.66−293326.48 [a]	1.684	21.85	44.84
DES J003948.24−445323.16 [a]	1.684	19.59	45.74
DES J003635.93−434636.05 [a]	1.689	19.90	45.62
DES J025220.53+002735.19 [a]	1.690	19.86	45.63

Table A3 – *continued*

DES ID	z	m_r	$\log(\lambda L_{1350})$ (erg s^{-1})
DES J021902.58−044628.33 [a]	1.694	19.92	45.61
DES J025356.07+001057.54 [a]	1.695	19.47	45.79
DES J003325.69−434826.13 [a]	1.696	20.26	45.48
DES J024527.72−010602.84 [a]	1.696	20.05	45.56
DES J022445.77−061149.99 [a]	1.701	20.19	45.51
DES J022014.98−062253.15 [a]	1.716	19.91	45.63
DES J024632.55−003439.14 [a]	1.724	19.87	45.65
DES J022134.97−070831.84 [a]	1.728	20.70	45.32
DES J032940.47−275143.61 [a]	1.730	19.87	45.66
DES J022602.20−061626.10 [a]	1.736	19.97	45.62
DES J003206.50−425325.23 [a]	1.750	19.84	45.68
DES J033814.33−294213.78 [a]	1.750	19.94	45.64
DES J033453.60−264121.34 [a]	1.751	20.14	45.56
DES J033817.74−290324.90 [a]	1.753	19.61	45.77
DES J022115.04−043155.51 [a]	1.757	21.33	45.09
DES J033452.89−265215.54 [a]	1.757	19.10	45.98
DES J022117.44−063856.45 [a]	1.763	19.83	45.69
DES J024257.19−004549.41 [a]	1.770	21.08	45.20
DES J022119.91−045948.62 [a]	1.770	20.76	45.32
DES J003120.86−425145.98 [a]	1.771	20.14	45.57
DES J004029.04−441704.97 [a]	1.783	20.04	45.62
DES J003255.12−435757.56 [a]	1.784	20.07	45.61
DES J032759.97−271921.90 [a]	1.785	20.37	45.49
DES J024222.95−011527.57 [a]	1.785	20.24	45.54
DES J033328.60−290314.66 [a]	1.787	19.58	45.80
DES J022027.32−045115.53 [a]	1.788	21.14	45.18
DES J022002.08−050101.91 [a]	1.791	19.69	45.76
DES J022751.50−044252.66 [a]	1.795	20.60	45.40
DES J003939.41−444612.90 [a]	1.797	20.17	45.58
DES J022503.11−065258.79 [a]	1.798	20.09	45.61
DES J032835.62−274406.09 [a]	1.800	19.94	45.67
DES J033722.89−274020.85 [a]	1.804	19.93	45.67
DES J003920.50−440441.16 [a]	1.814	19.79	45.74
DES J003739.59−432521.40 [a]	1.815	20.40	45.49
DES J024635.61−000850.46 [a]	1.822	19.26	45.95
DES J033002.51−274858.28 [a]	1.823	20.70	45.38
DES J033548.18−290943.65 [a]	1.826	20.33	45.53
DES J022352.09−064029.96 [a]	1.827	20.50	45.46
DES J022409.89−044718.00 [a]	1.832	20.11	45.62
DES J033319.58−290431.65 [a]	1.833	20.73	45.37
DES J024716.32−010401.36 [a]	1.834	21.10	45.23
DES J033222.47−285935.09 [a]	1.837	20.68	45.40
DES J033301.69−275818.80 [a]	1.840	20.94	45.29
DES J004014.18−431716.29 [a]	1.842	19.87	45.72
DES J021903.49−043935.00 [a]	1.845	20.48	45.48
DES J024737.50−000458.97 [a]	1.847	19.88	45.72
DES J024608.67−013933.97 [a]	1.848	19.68	45.80
DES J022515.35−044008.91 [a]	1.850	19.82	45.75
DES J025038.68−004739.06 [a]	1.856	18.67	46.21
DES J002729.28−431501.02 [a]	1.863	19.67	45.81
DES J024723.54−002536.48 [a]	1.864	19.42	45.92
DES J022845.57−043350.18 [a]	1.864	17.41	46.72
DES J024748.87−000147.41 [a]	1.868	19.58	45.85
DES J024133.65−010724.20 [a]	1.874	20.86	45.34
DES J003940.80−443718.32 [a]	1.875	19.49	45.89
DES J022047.63−051835.83 [a]	1.878	19.55	45.87
DES J021707.96−055152.07 [a]	1.885	19.70	45.82
DES J033145.20−275435.75 [a]	1.891	21.19	45.22
DES J024242.50−002212.87 [a]	1.904	20.57	45.48
DES J022828.19−040044.25 [a]	1.905	18.31	46.38
DES J003626.44−430820.66 [a]	1.907	19.80	45.79
DES J022050.39−061748.80 [a]	1.908	21.89	44.95
DES J021953.45−061123.39 [a]	1.910	19.90	45.75

Table A3 – *continued*

DES ID	z	m_r	$\log(\lambda L_{1350})$ (erg s^{-1})
DES J003150.13−432726.88 [a]	1.912	18.68	46.24
DES J022328.88−040134.71 [a]	1.915	19.82	45.78
DES J033739.88−272045.97 [a]	1.916	19.21	46.03
DES J033924.44−271250.15 [a]	1.918	20.52	45.51
DES J025428.31+002418.43 [a]	1.918	20.42	45.55
DES J033415.37−265535.62 [a]	1.922	19.85	45.78
DES J033011.77−283636.65 [a]	1.922	20.99	45.32
DES J022327.85−040119.16 [a]	1.922	20.81	45.39
DES J024639.22−012731.85 [a]	1.923	20.34	45.58
DES J022250.47−060104.89	1.925	21.54	45.10
DES J022206.47−060746.70	1.927	20.89	45.36
DES J022514.39−044700.14	1.928	18.83	46.19
DES J034005.69−292312.82	1.928	19.04	46.10
DES J033701.63−282753.94	1.933	20.20	45.64
DES J034016.06−270925.57	1.935	19.72	45.84
DES J033832.50−291215.65	1.935	20.77	45.41
DES J022537.03−050109.34	1.936	20.03	45.71
DES J033316.17−292917.48	1.947	19.95	45.75
DES J033607.36−263207.88	1.948	20.02	45.72
DES J033401.79−265054.28	1.952	19.72	45.84
DES J033232.00−280309.98	1.954	19.98	45.74
DES J025233.79+004340.74	1.954	20.60	45.49
DES J033646.40−291617.17	1.956	20.47	45.54
DES J033052.19−274926.84	1.958	21.49	45.14
DES J033559.60−280324.41	1.965	20.60	45.49
DES J024918.63+000548.34	1.966	20.66	45.47
DES J033650.66−293142.07	1.972	21.68	45.06
DES J032926.49−271844.01	1.978	20.33	45.61
DES J021949.99−064208.13	1.984	19.93	45.77
DES J033839.06−292351.17	1.987	20.33	45.61
DES J025159.70−005159.89	1.988	21.84	45.01
DES J022812.23−043227.58	1.992	21.04	45.33
DES J004016.18−435116.09	1.995	19.98	45.75
DES J033912.95−273516.85	2.006	20.08	45.72
DES J032821.07−282055.17	2.011	19.50	45.95
DES J022352.19−043031.68	2.012	19.75	45.85
DES J033040.28−274203.95	2.013	19.96	45.77
DES J022657.24−035944.42	2.018	20.17	45.68
DES J025019.26+003100.81	2.018	20.26	45.65
DES J022530.19−065458.19	2.030	19.49	45.96
DES J032703.62−274425.27	2.031	19.45	45.98
DES J022034.93−052956.02	2.036	18.20	46.48
DES J034036.10−284811.29	2.039	20.13	45.71
DES J022629.26−043057.07	2.040	20.18	45.69
DES J002959.21−434835.24	2.041	17.77	46.65
DES J022045.50−045121.91	2.045	19.92	45.80
DES J021935.78−064227.17	2.060	21.83	45.04
DES J003146.74−423601.03	2.061	19.54	45.95
DES J033635.40−280828.78	2.067	20.28	45.66
DES J021905.63−055958.78	2.069	20.11	45.73
DES J003549.05−440236.08	2.072	19.23	46.08
DES J021957.25−043952.46	2.077	18.90	46.22
DES J004143.04−440234.42	2.081	20.32	45.65
DES J024453.25−011256.33	2.083	20.73	45.49
DES J024344.30−000201.08	2.083	20.04	45.77
DES J032602.35−281031.00	2.085	20.01	45.78
DES J021850.07−050954.10	2.091	19.52	45.98
DES J021921.81−043642.21	2.092	20.04	45.77
DES J021941.16−044100.36	2.096	21.15	45.33
DES J033015.97−280219.79	2.097	20.18	45.72
DES J004022.52−442820.25	2.100	19.42	46.02
DES J024431.59−052818.78	2.102	17.53	46.78
DES J024628.49−004457.13	2.104	19.94	45.81

Table A3 – *continued*

DES ID	z	m_r	$\log\left(\lambda L_{1350}\right)$ (erg s^{-1})
DES J003848.52−440202.07	2.105	19.72	45.90
DES J024357.91−005447.75	2.105	21.03	45.38
DES J022044.45−050905.95	2.108	21.19	45.32
DES J025209.79+000549.21	2.108	19.95	45.81
DES J024756.35−001555.92	2.119	18.70	46.32
DES J022813.61−042251.65	2.121	19.63	45.95
DES J033640.29−284423.00	2.124	20.80	45.48
DES J024739.11−005221.01	2.124	20.50	45.60
DES J022411.52−060915.92	2.128	19.82	45.87
DES J024550.79−004328.13	2.131	20.52	45.59
DES J003816.16−434647.44	2.141	19.54	45.99
DES J003936.81−443439.72	2.144	19.97	45.82
DES J022219.46−062539.66	2.146	19.04	46.19
DES J032829.96−274212.23	2.150	20.12	45.76
DES J024632.44−003214.12	2.152	18.89	46.25
DES J021441.86−043709.03	2.152	22.17	44.94
DES J022028.95−045802.58	2.153	20.53	45.60
DES J033326.24−275829.85	2.161	20.53	45.60
DES J022351.07−044729.93	2.163	20.93	45.44
DES J033217.15−271956.41	2.169	19.24	46.12
DES J032923.16−280022.78	2.175	19.77	45.91
DES J002913.21−433044.56	2.180	20.11	45.78
DES J025335.12−003039.26	2.184	20.41	45.66
DES J032939.97−284952.40	2.188	20.22	45.73
DES J024557.22−000823.36	2.199	20.05	45.81
DES J022001.63−052216.92	2.219	20.17	45.77
DES J003320.08−430428.45	2.231	20.19	45.76
DES J024840.78−003548.15	2.235	18.89	46.28
DES J022358.64−045351.63	2.235	20.29	45.72
DES J003448.83−442519.26	2.237	20.13	45.79
DES J033852.79−282256.93	2.246	19.78	45.93
DES J022402.32−061740.34	2.246	19.91	45.88
DES J002907.77−420916.39	2.247	20.77	45.54
DES J024907.29−000649.35	2.251	20.31	45.72
DES J003743.89−434715.68	2.257	19.60	46.01
DES J022725.81−033837.75	2.257	18.20	46.57
DES J021757.52−045059.15	2.257	20.73	45.56
DES J003516.08−432451.82	2.260	19.47	46.06
DES J022557.62−045005.32	2.271	19.55	46.03
DES J022229.62−044941.93	2.275	21.22	45.37
DES J033604.00−274203.95	2.277	21.41	45.29
DES J022729.22−043227.66	2.280	19.75	45.96
DES J033655.83−290218.23	2.283	19.41	46.09
DES J024204.58−003835.64	2.287	20.21	45.77
DES J022451.98−041210.79	2.294	20.14	45.80
DES J022612.64−043401.32	2.306	21.08	45.43
DES J022748.85−042820.90	2.311	20.08	45.84
DES J022410.96−050653.95	2.315	20.66	45.60
DES J024950.74−004224.16	2.317	20.45	45.69
DES J024520.05−004534.45	2.321	20.79	45.55
DES J021730.92−041823.54	2.322	19.75	45.97
DES J033843.76−294922.54	2.328	20.67	45.60
DES J022824.68−041545.71	2.328	19.63	46.02
DES J003436.78−440043.41	2.330	19.58	46.04
DES J025128.73−002650.64	2.330	19.95	45.89
DES J022055.10−061842.21	2.340	21.09	45.44
DES J024337.15−002340.17	2.347	19.36	46.14
DES J033822.77−275910.73	2.349	19.64	46.02
DES J024505.03−003441.97	2.350	20.60	45.64
DES J025033.20+003829.22	2.364	19.96	45.90
DES J004056.56−431446.40	2.384	19.56	46.07
DES J033734.80−294213.92	2.390	19.84	45.96

Table A3 – *continued*

DES ID	z	m_r	$\log\left(\lambda L_{1350}\right)$ (erg s^{-1})
DES J033953.34−270053.36	2.410	18.53	46.49
DES J003430.47−433311.36	2.415	20.75	45.60
DES J025102.06−004142.78	2.425	22.15	45.05
DES J032942.28−281906.69	2.436	20.42	45.74
DES J033605.57−290354.17	2.450	20.17	45.85
DES J022354.81−044814.94	2.452	18.74	46.42
DES J022014.33−042917.10	2.458	19.30	46.20
DES J024511.94−011317.50	2.462	20.46	45.74
DES J024757.67+001542.65	2.467	20.87	45.57
DES J033430.30−275958.91	2.472	21.32	45.40
DES J022540.58−043825.15	2.477	20.27	45.82
DES J032640.93−283206.80	2.492	20.28	45.82
DES J024717.40−000052.27	2.497	20.30	45.81
DES J003017.36−423144.34	2.497	20.00	45.93
DES J003957.42−434107.92	2.500	20.14	45.88
DES J033237.62−271448.07	2.519	20.30	45.82
DES J033608.10−285245.81	2.522	20.30	45.82
DES J003145.23−424618.45	2.523	20.70	45.66
DES J033545.52−275451.69	2.540	20.28	45.83
DES J003341.34−420811.51	2.541	19.80	46.02
DES J033216.69−272411.37	2.547	19.77	46.04
DES J022259.87−063326.65	2.563	20.60	45.71
DES J003547.38−430558.81	2.565	20.03	45.94
DES J022434.33−043200.27	2.568	20.06	45.93
DES J033518.30−275304.01	2.576	19.33	46.22
DES J003530.07−444539.88	2.587	20.06	45.93
DES J003352.72−425452.55	2.593	19.10	46.32
DES J033331.37−275634.38	2.602	20.37	45.81
DES J024719.59−003313.11	2.607	20.48	45.77
DES J032739.71−281934.84	2.616	20.18	45.89
DES J034121.52−265901.04	2.621	19.44	46.19
DES J021457.21−043011.44	2.636	18.34	46.63
DES J022104.88−060728.52	2.648	20.05	45.95
DES J022631.82−045127.47	2.655	20.77	45.66
DES J022330.15−043004.09	2.677	20.78	45.66
DES J021719.45−052305.27	2.695	19.36	46.23
DES J022034.52−045132.47	2.732	20.40	45.83
DES J033944.09−284604.07	2.744	19.33	46.27
DES J022620.86−045946.48	2.745	21.30	45.48
DES J025223.48−003623.57	2.769	20.20	45.93
DES J025236.38−285747.93	2.770	18.08	46.78
DES J033938.51−291019.54	2.778	21.16	45.55
DES J021921.22−044315.03	2.794	20.17	45.95
DES J022636.07−043428.92	2.801	19.88	46.07
DES J022354.85−054839.89	2.814	19.31	46.30
DES J021659.87−053203.49	2.818	17.60	46.99
DES J022305.97−054015.26	2.823	20.04	46.01
DES J022321.26−055600.27	2.846	21.55	45.42
DES J022255.51−044410.32	2.871	20.31	45.92
DES J033720.58−272434.70	2.896	20.16	45.99
DES J003255.24−430948.41	3.010	19.57	46.26
DES J022423.43−070627.92	3.030	21.48	45.50
DES J003318.29−434301.10	3.082	19.31	46.38
DES J033246.76−280846.78	3.180	19.17	46.47
DES J021438.15−052024.38	3.214	20.93	45.77
DES J025250.10+000830.68	3.237	20.27	46.04
DES J003133.50−422953.97	3.248	20.62	45.90
DES J021906.24−041933.94	3.330	21.60	45.54
DES J033712.16−285146.74	3.364	20.33	46.06
DES J003411.44−424329.48	3.373	20.83	45.86
DES J002926.44−420752.35	3.403	19.71	46.32
DES J022543.53−042834.48	3.411	20.64	45.95

Table A3 – *continued*

DES ID	z	m_r	$\log(\lambda L_{1350})$ (erg s^{-1})
DES J024325.96−003145.11	3.435	19.63	46.36
DES J022133.35−065713.47	3.440	20.16	46.15
DES J034122.60−291302.04	3.470	20.33	46.09
DES J033512.61−292351.14	3.712	19.98	46.27
DES J024509.76−010001.28	3.807	20.58	46.05
DES J022144.21−062745.18	3.856	20.14	46.24

APPENDIX B: Hβ EXCLUDING OBJECTS WITH INDIVIDUAL LAGS

The luminosity bins for the Hβ sample excluding sources with individual lags are shown in Fig. B1, and the stacked CCF's and average lags for this reduced sample are given in Figs B2 and B3. Only the two lowest (blue and orange) and second highest (red) luminosity bins had objects excluded. The stacked CCF peaks remain intact for each of these bins, although the signal to noise degrades slightly, which is to be expected as the size of the stacked sample decreased by ∼one sixth. The average lags are in close agreement to those recovered in the original analysis in
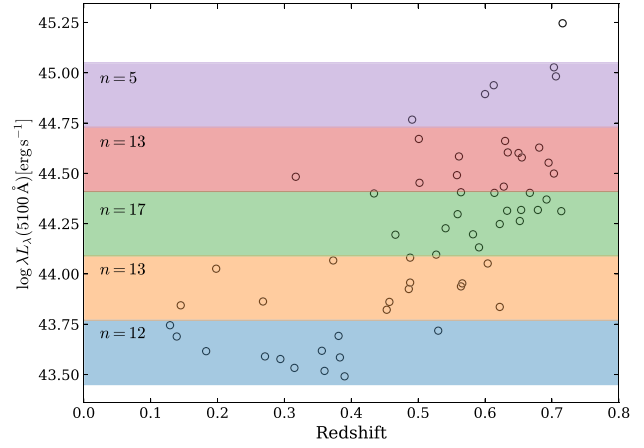

Figure B1. The same as Fig. 2 after excluding sources with individual lag recoveries.

Section 4. This test indicates that the results from stacking are not dominated by objects with high quality individual lags, although their addition does considerably improve the lag uncertainties for the final result.
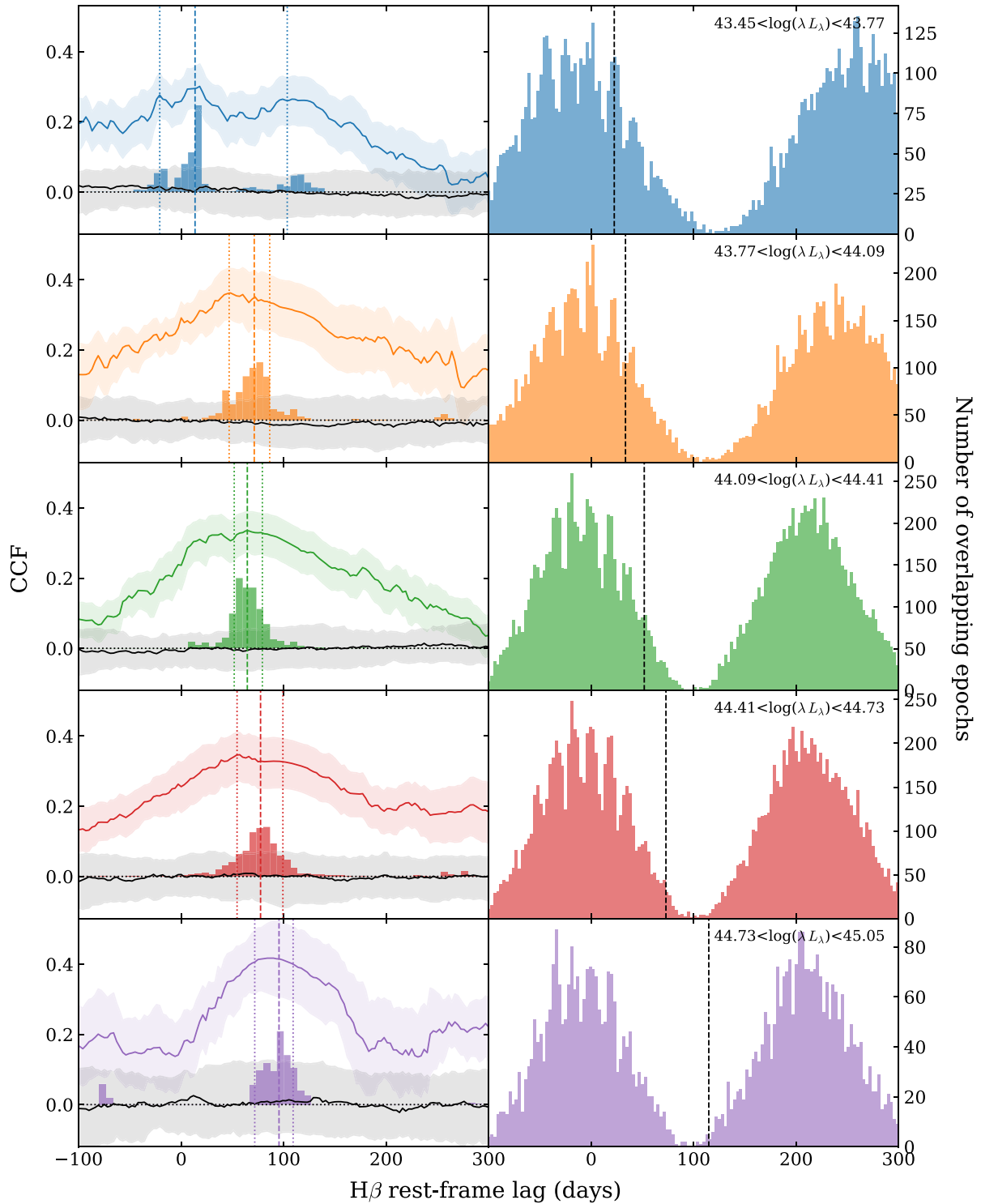
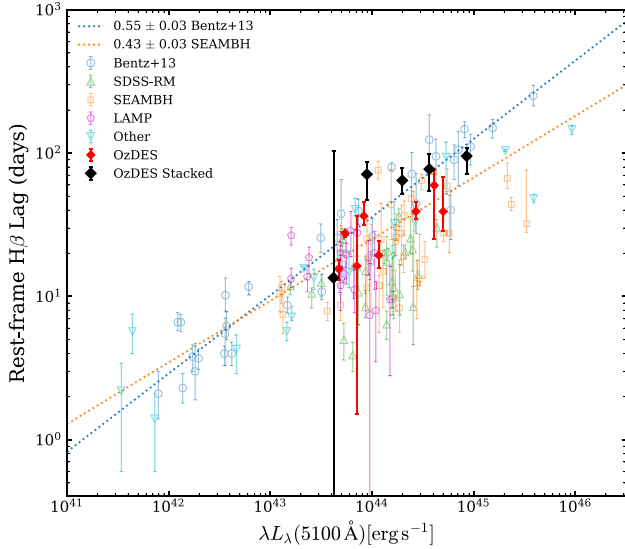**Figure B2.** The same as Fig. 3 after excluding sources with individual lag recoveries from the stacked sample.

Figure B3. The Radius–Luminosity relation for Hβ (dotted lines), including the stacked average lag measurements made using the OzDES Hβ sample after excluding sources with individual lag recoveries, and existing individual lag measurements (same as in Fig. 4).

[1]*Research School of Astronomy and Astrophysics, Australian National University, Canberra, ACT 2611, Australia*

[2]*School of Mathematics and Physics, The University of Queensland, St Lucia, QLD 4101, Australia*

[3]*Department of Astronomy, The Ohio State University, Columbus, Ohio 43210, USA*

[4]*Center of Cosmology and Astro-Particle Physics, The Ohio State University, Columbus, Ohio 43210, USA*

[5]*National Centre for the Public Awareness of Science, Australian National University, Canberra, ACT 2601, Australia*

[6]*The Australian Research Council Centre of Excellence for All-Sky Astrophysics in 3 Dimension (ASTRO 3D), Australia*

[7]*Sydney Institute for Astronomy, School of Physics, The University of Sydney, NSW 2006, Australia*

[8]*Centre for Gravitational Astrophysics, College of Science, The Australian National University, ACT 2601, Australia*

[9]*Laboratório Interinstitucional de e-Astronomia—LIneA, Rua Gal. José Cristino, Rio de Janeiro, RJ 20921–400, Brazil*

[10]*Department of Physics, University of Michigan, Ann Arbor, MI 48109, USA*

[11]*Fermi National Accelerator Laboratory, PO Box 500, Batavia, IL 60510, USA*

[12]*Departamento de Física Teórica and Instituto de Física de Partículas y del Cosmos (IPARCOS-UCM), Universidad Complutense de Madrid, E-28040 Madrid, Spain*

[13]*Institute of Cosmology and Gravitation, University of Portsmouth, Portsmouth, PO1 3FX, UK*

[14]*Department of Physics & Astronomy, University College London, Gower Street, London, WC1E 6BT, UK*

[15]*Instituto de Astrofisica de Canarias, E-38205 La Laguna, Tenerife, Spain*

[16]*Universidad de La Laguna, Dpto. Astrofísica, E-38206 La Laguna, Tenerife, Spain*

[17]*Institut de Física d'Altes Energies (IFAE), The Barcelona Institute of Science and Technology, Campus UAB, E-08193 Bellaterra (Barcelona), Spain*

[18]*Centre for Extragalactic Astronomy, Durham University, South Road, Durham, DH1 3LE, UK*

[19]*Hamburger Sternwarte, Universität Hamburg, Gojenbergsweg 112, D-21029 Hamburg, Germany*

[20]*Centro de Investigaciones Energéticas, Medioambientales y Tecnológicas (CIEMAT), Madrid 28040, Spain*

[21]*Institute of Theoretical Astrophysics, University of Oslo, PO Box 1029 Blindern, NO-0315 Oslo, Norway*

[22]*Kavli Institute for Cosmological Physics, University of Chicago, Chicago, IL 60637, USA*

[23]*University Observatory, Faculty of Physics, Ludwig-Maximilians-Universität, Scheinerstr 1, D-81679 Munich, Germany*

[24]*Center for Astrophysical Surveys, National Center for Supercomputing Applications, 1205 West Clark St, Urbana, IL 61801, USA*

[25]*Department of Astronomy, University of Illinois at Urbana-Champaign, 1002 W. Green Street, Urbana, IL 61801, USA*

[26]*Santa Cruz Institute for Particle Physics, Santa Cruz, CA 95064, USA*

[27]*Center for Astrophysics | Harvard & Smithsonian, 60 Garden Street, Cambridge, MA 02138, USA*

[28]*Australian Astronomical Optics, Macquarie University, North Ryde, NSW 2113, Australia*

[29]*Lowell Observatory, 1400 Mars Hill Rd, Flagstaff, AZ 86001, USA*

[30]*George P. and Cynthia Woods Mitchell Institute for Fundamental Physics and Astronomy, and Department of Physics and Astronomy, Texas A&M University, College Station, TX 77843, USA*

[31]*Institució Catalana de Recerca i Estudis Avançats, E-08010 Barcelona, Spain*

[32]*Observatório Nacional, Rua Gal. José Cristino 77, Rio de Janeiro, RJ 20921–400, Brazil*

[33]*Department of Physics, Carnegie Mellon University, Pittsburgh, Pennsylvania 15312, USA*

[34]*Kavli Institute for Particle Astrophysics & Cosmology, PO Box 2450, Stanford University, Stanford, CA 94305, USA*

[35]*SLAC National Accelerator Laboratory, Menlo Park, CA 94025, USA*

[36]*Department of Physics and Astronomy, Pevensey Building, University of Sussex, Brighton, BN1 9QH, UK*

[37]*School of Physics and Astronomy, University of Southampton, Southampton, SO17 1BJ, UK*

[38]*Computer Science and Mathematics Division, Oak Ridge National Laboratory, Oak Ridge, TN 37831, USA*

[39]*Lawrence Berkeley National Laboratory, 1 Cyclotron Road, Berkeley, CA 94720, USA*

This paper has been typeset from a TeX/LaTeX file prepared by the author.